Evolution of the Monterey Bay Sea-Breeze Layer As Observed by Pulsed Doppler Lidar

ROBERT M. BANTA, LISA D. OLIVIER, AND DAVID H. LEVINSON*

NOAA/ERL Wave Propagation Laboratory, Boulder, Colorado

(Manuscript received 15 June 1992, in final form 11 March 1993)

ABSTRACT

As part of the Land/Sea Breeze Experiment (LASBEX) to study the sea breeze at Monterey Bay, the pulsed Doppler lidar of the NOAA/ERL Wave Propagation Laboratory performed vertical and nearly horizontal scans of the developing sea breeze on 12 days. Analyses of Doppler velocity data from these scans revealed details on the growth of the sea-breeze layer and on the horizontal variability of the sea breeze resulting from inland topography. Two days were selected for study when the ambient flow was offshore, because the onshore flow of the sea breeze was easy to discern from the background flow. Sequences of vertical cross sections taken perpendicular to the coast showed the beginnings of the sea breeze beneath the land breeze at the coast and the subsequent growth of the sea-breeze layer horizontally and vertically. On one of the days a transient precursor—a "minor sea breeze"—appeared and disappeared before the main sea breeze began in midmorning. Other issues that the lidar was well suited to study were the compensating return flow, the Coriolis effect, the effects of topography, and the growth of the dimensions of the sea-breeze layer. No return flow above the sea breeze and no Coriolis turning of the sea-breeze flow were found even through the late afternoon hours. Terrain effects included an asymmetry in the development of the sea breeze over water as opposed to over land and the persistence into the late morning hours of southeasterly flow from the Salinas River valley toward the vicinity of the lidar. Vertical and horizontal dimensions of the sea-breeze layer were determined from lidar vertical cross sections. From these, length-to-width aspect ratios were calculated, which were then compared with aspect ratios derived from recent analytical models. The theoretical values compared poorly with the observed values, most likely because the complicating effects of topography and stability were not accounted for in the theoretical models.

1. Introduction

If the sea breeze is not the most studied atmospheric phenomenon, it is certainly one of the most. One reason for this is that the world's population is heavily concentrated along the coasts of oceans and major lakes such as the Great Lakes of the north-central United States. This means both that there are practical reasons for studying the sea breeze and that there is a population of meteorologists living in coastal areas who try to make sense out of local weather phenomena. A second reason is that the geometry of the sea breeze is straightforward: the flow forms at the boundary between a region with a warm surface and one with a cool surface. This simple basic structure makes the sea breeze a logical subject for numerical modeling studies in two dimensions, as pursued by Estoque (1961, 1962) and many others since then, and in three dimensions, as pursued by Pielke (1974) and others since. It is similarly a logical subject for theoretical investigations. Rotunno (1983) presented a nice review of progress in analytical models as it pertained to his own study, and more recently Dalu and Pielke (1989) built on Rotunno's results.

These modeling studies have had an extensive background of observational studies with which to compare (Atkinson 1981; Pielke 1984). With all the observational attention already paid to this problem, one might well ask, what is there left to contribute? As pointed out in the recent National Research Council (NRC) review on coastal meteorology (National Research Council 1992), a number of important aspects of the sea breeze are still poorly understood. In this study we address some of these issues:

1) The seaward extent of the sea breeze has been poorly documented, as pointed out recently by Arritt (1989), although many observational studies have focused on its inland penetration.

2) The relationship between the sea breeze and inland topography, which also generates daytime upslope flows, is not well understood.

3) The compensatory return flow above the sea-breeze layer, claimed to be required for mass continuity in many modeling studies, has been difficult to find in many observational studies.

Other poorly understood issues cited in the NRC report include the land breeze, the structure and magnitude

* Current affiliation: CIRES, University of Colorado, Boulder, Colorado.

Corresponding author address: Dr. Robert Banta, NOAA/ERL: R/EWP2, 325 Broadway, Boulder, CO 80303-3328.

of vertical velocity associated with the sea and land breeze system, and the offshore structure of both the land and sea breeze.

One reason these issues have not been resolved is that the instrumentation systems used in many of the previous studies, which have provided considerable insight into the behavior of the sea breeze, have reached some fundamental limitations. Accessibility is a problem: it is difficult and expensive to obtain vertical profiles of atmospheric variables over water with in situ sensors, and it is generally expensive to obtain even surface data there, for example, by ship or buoy. Over land, surface meteorological stations and towers can give excellent records of meteorological variables at fine time resolution, but vertical extent is limited. Balloon-borne instruments have given needed vertical profile information, but many of the equivocal results on the presence of return-flow layers, for example, arise from the coarse time and space resolutions of these kinds of observations. Wind profiles from balloon ascents taken even as frequently as intervals of 20 to 30 min in time and 50 km or greater in space cannot show convincingly that a layer, such as a return-flow layer, is absent. Hesitant to assert that their data show no return flow, studies often conclude with statements such as, "The return flow was difficult to detect because of the overriding gradient flow" (Frizzola and Fischer 1963, p. 738) and "The return current predicted by theory has not always been observed. . . . Perhaps one of the reasons . . . is that instruments were simply not sent high enough: it was the sea breeze *per se* that claimed attention, not the overlying return current" (Atkinson 1981). Thus, although there have been observational studies in which return flows do not appear in the data, authors have been reluctant to conclude that these flows were not there.

A similar problem exists for topographical effects: the spatial density of in situ measurements necessary to observe such effects can easily be prohibitive in very complex inland terrain.

In the present study we address some of these issues using new technology, the Doppler lidar developed by the Wave Propagation Laboratory (WPL) of the National Oceanic and Atmospheric Administration's (NOAA) Environmental Research Laboratories (ERL). The lidar is ideally suited to study many of these issues because of its scanning capability. Vertical scans performed perpendicular to the coastline provide vertical two-dimensional slices of the component of flow perpendicular to the coastline. These vertical slices can give definitive answers about the existence or absence of layers, about the vertical growth of the sea-breeze layer, and about the horizontal extent of the layers (to the maximum range of the instrument). The lidar can also perform nearly horizontal scans (rotating in azimuth at fixed elevation angles less than 5°) to study the horizontal variability of the flow. Full 360° azimuthal scans at any elevation angle also provide vertical profiles of the horizontal wind using techniques discussed in section 2a. These scans, which take less than 2 min to perform, can provide frequent wind profiles centered on the lidar.

This study is the first time that pulsed Doppler lidar has been used to study the sea breeze, but it is not the first time that remote sensing instruments have been used to observe sea-breeze phenomena. For example, Atlas (1960) used a Doppler radar to study the sea breeze off the coast of Massachusetts, and Meyer (1971) used Doppler radar to determine the offshore extent of the land breeze off the coast of Wallops Island, Virginia. Fett and Tag (1984) employed satellite imagery to infer the offshore extent of the sea breeze by observing differences in wave reflectivity of sunlight. Nakane and Sasano (1986) used backscatter data from a high-powered non-Doppler lidar in Japan to observe the finescale structure of a sea-breeze front as it moved inland, and Wakimoto and McElroy (1986) used backscatter data from an airborne lidar to study the sea breeze and other flows in the Los Angeles Basin. In addition, a number of studies have used sodar.

We investigate here the sea breeze along the central California coast at Monterey Bay. The sea breeze along the Pacific coast of the western United States (northward from central California) differs from that in areas where many other sea-breeze studies have been conducted because of the very strong marine inversion at the coast and offshore. The strong inversion is produced by the combination of cold, upwelling surface waters just offshore (Johnson and O'Brien 1973) and lower-tropospheric subsidence under the subtropical high pressure system. This surface high persists over the Pacific Ocean west of southern California during the warm season. Other features special to this area are the coastal mountain ranges and the hot interior valleys. The strong temperature gradient between these hot valleys and the cold waters offshore gives rise to a northerly to north-northwesterly geostrophic flow along the coast, which produces cross-isobaric, onshore flow at low levels. This onshore flow is so typical of warm-season days that Fosberg and Schroeder (1966) and Schroeder et al. (1967) referred to it as a "monsoon."

In order to understand this "sea breeze in an upwelling regime" (as described by Johnson and O'Brien 1973), the Land/Sea Breeze Experiment (LASBEX) was conducted in September 1987 (Intrieri et al. 1990). A combination of high-resolution remote sensors and conventional in situ instruments obtained detailed measurements of the sea-breeze circulation. The remote sensing instruments included WPL's Doppler lidar and Doppler sodars as described by Fagan (1988). Conventional instrumentation consisted of surface mesonet stations and radiosonde.

In section 2 of this paper we discuss the LASBEX project, including the terrain and the synoptic weather patterns encountered, and the instrumentation used, with emphasis on the lidar. We use surface station data to stratify the LASBEX study days into three categories: days with an abrupt sea-breeze frontal passage and off-

shore ambient flow, days with a gradual frontal passage and onshore ambient flow, and days with intermediate characteristics. These categories correspond to the three types of day noted by Fosberg and Schroeder (1966). In section 3 we present lidar analyses of the evolution of the sea-breeze flow layer on the days with an offshore ambient wind flow. The sea breeze on these days was best defined and most easily distinguishable from the background flow. In section 4 we focus on the issues of return flow, initiation of onshore flow, growth in the dimensions of the sea-breeze layer over the coast and offshore, and the absence of Coriolis turning in the Monterey Bay sea breeze. The final section presents our summary and conclusions.

2. The Land/Sea Breeze Experiment

LASBEX was conducted on the central coast of California at Monterey Bay, near the towns of Moss Landing and Castroville, from 15 to 30 September 1987. The purpose, scope, and some preliminary results of the experiment were described by Intrieri et al. (1990). Figure 1 shows the surrounding terrain and location of the sensors. In addition to the instrumentation deployed over land, a ship, the R/V *Silver Prince,* served as a platform for surface observations and rawinsonde ascents during daylight hours on eight weekdays during LASBEX. As discussed in section 1, the experiment featured two kinds of remote sensing instruments, WPL's Doppler lidar and an array of Doppler sodars. To supplement the remote sensing observations, six surface mesonet stations and two radiosonde sites, one near Castroville and the other on the *Silver Prince,* were deployed as a part of LASBEX, as discussed in the next subsection. We also used data from a number of surface stations already existing in the Monterey Bay area, shown on Fig. 1.

a. Doppler lidar

The Doppler lidar was stationed 1.5 km east of Monterey Bay. From this location, it was able to scan over land and water. A lidar is a remote sensing instrument similar to a radar, except that lidar transmits a pulse of light instead of radio frequency waves. The lidar in the present study, developed by WPL, transmits eye-safe infrared (IR) light. Characteristics of the lidar as used during LASBEX are listed in Table 1.

The transmitted beam is scattered by atmospheric aerosols, and a small fraction of the scattered energy is received back at the instrument. From this returned signal two kinds of information are processed by the lidar's computers: backscattered intensity, which is a function of the size, shape, concentration, and refractive index of the scatterers, and the Doppler-shifted frequency of the returned signal, which provides an estimate of the component of the wind directed away from the lidar. In this paper, we refer to this lidar-centered radial component of the wind as the "radial wind" u_r, with positive values indicating a positive Doppler shift, that is, flow away from the lidar. Backscatter data are not presented in this paper.

Our signal-processing equipment gives these two kinds of information (backscattered intensity and u_r) averaged over discrete range intervals of 300 m, from a minimum range of 1.2 km to a maximum range of up to 30 km, depending on atmospheric attenuation conditions. Both high absolute humidities and low atmospheric aerosol concentrations (i.e., a clean atmosphere) restrict the lidar's range. During the LASBEX project the lidar range was generally between 10 and 15 km. Because the lidar beam is strongly attenuated by cloud droplets, clouds and fog with significant liquid water content are essentially opaque to the lidar. In the present data this characteristic showed up as a dropout of the signal when fog or stratus clouds intercepted the beam.

The diameters of the aerosols that scatter most of the energy back to the lidar are typically 1–3 μm. This was determined from Mie calculations for 10.6-μm radiation using observed normal atmospheric aerosol size distributions (Post 1978; Banta et al. 1992). Aerosols in this size range have negligible fall speeds, and thus are excellent tracers of atmospheric flow for the small-scale wind systems studied here.

The technical attributes of the current lidar system were described most recently by Post and Cupp (1990), with many of the important characteristics tabulated. Significantly, the beam is very narrow, with a 90-μrad (0.005°) field of view (it is thus only $\sim$1 m wide at a range of 11 km), and it does not have side lobes. These two characteristics make the lidar a remote sensing tool especially well suited to studying flow close to the earth's surface. This advantage is even greater in complex terrain. Other recent reviews of the characteristics of the WPL lidar and of atmospheric measurement projects that have demonstrated the unique capabilities of the lidar were given by Menzies and Hardesty (1989), Hardesty et al. (1987), Hardesty et al. (1988), and Hardesty et al. (1991).

Two final lidar issues are scanning and the resolution of the observations. The lidar system has the capability to scan either in azimuth or elevation. The most useful scans during LASBEX were vertical slices or cross sections of the atmosphere, which revealed the layered structure of the flow. These scans, referred to in radar terminology as range–height indicator (RHI) scans, were produced by scanning in elevation angle at a fixed azimuth. The most common vertical cross sections were east–west (90°/270° azimuth), because these scans were perpendicular to the coast and thus parallel to the sea-breeze flow. They showed the vertical structure of the sea-breeze circulation from the surface of the land and water to the top of the aerosol layer several (usually 3–5) kilometers above the surface. We also took other RHI scans along the 140°/320° azimuth to measure wind flow toward the Salinas River valley and out over the water to the northwest, and along the

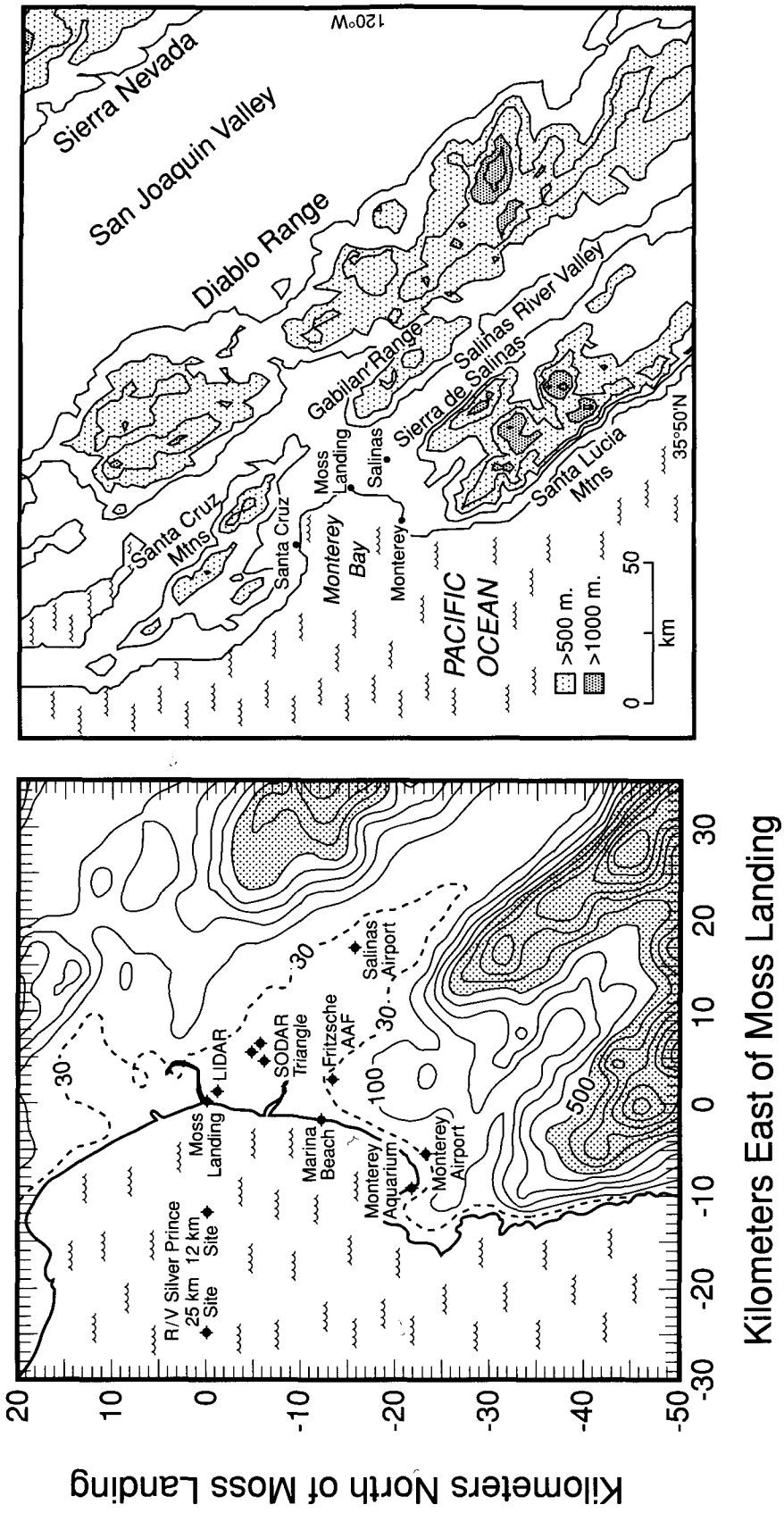

FIG. 1. Maps of the LASBEX experiment site. (a) Locations of sensors and sites with routine surface meteorological measurements. The dashed terrain contour is 30 m above sea level. Solid terrain contours are at 100-m intervals. Terrain above 500 m is shaded (adapted from Fagan 1988). Castroville is located just northwest of the northern vertex of the sodar triangle. (b) Larger-scale map of the region. Mountain ranges and valleys impacting the coastal wind flows are shown. Terrain above 500 m has light shading and terrain greater than 1000 m has dark shading.

TABLE 1. Lidar specifications and parameters for LASBEX.

Lidar Specifications and Parameters for LASBEX	
Lidar specifications	
Wavelength (μm)	10.59
Maximum range (km)	up to 30.00
Minimum range (km)	1.20
Range resolution (km)	0.30
Beamwidth (μrad) [°]	90.00 [.005]
Rms velocity accuracy (cm s^{-1})	60.00
Pulse repetition frequency (Hz)	10.00
Pulses averaged	3.00
Effective pulse rate (Hz)	3.33
Scan parameters	
PPI scan rate (°s^{-1})	3.33
angular resolution (°)	1.00
RHI scan rate	
below 7.5° elevation (°s^{-1})	0.66
angular resolution (°)	0.20
above 7.5° elevation (°s^{-1})	3.33
angular resolution (°)	1.00

0°/360° azimuth (north–south) to show the alongcoast variability.

The lidar also scanned in azimuth at constant elevation angles; these scans are called plan position indicator (PPI) scans by radar meteorologists. At low elevation angles (less than ~10°), these scans can often be considered quasi-horizontal, especially in the absence of strong vertical layering. Under such conditions they provide good indications of the horizontal variability of the flow. During LASBEX these low-elevation scans thus revealed information about the spatial variability of the sea breeze and land breeze, especially as they were affected by the terrain.

At higher elevation angles, scans in azimuth give information on the vertical structure of the flow. These scans, which represent cones of data in the atmosphere centered on the lidar scanner, can be used to determine vertical profiles of the mean horizontal wind by the velocity–azimuth display (VAD) technique, as described by Browning and Wexler (1968). Hall et al. (1984) found the accuracy of the winds in these profiles to be 34 cm s^{-1} when compared with tower measurements. The VAD technique can also be applied to the lower-elevation scans to produce high-resolution profiles of the horizontal wind near the surface. Caution is necessary in interpreting horizontal winds from these scans, since the algorithm used to compute the winds assumes a constant wind across the circle of u_r observations from which the horizontal wind is calculated. However, experience in comparing wind profiles from low-angle VAD scans with those from other sources, such as tethersondes, rawinsondes, and UHF profilers, has shown good agreement even under conditions of moderate horizontal variability. In this study we present VAD wind profiles based on PPI scans at 1° and 5° to show the evolution of the sea breeze.

An awareness of the resolution of the lidar data is important in interpreting properly the lidar cross sections and scans presented in this paper. This issue consists of two aspects: the resolution at which data were taken by the lidar (in spherical coordinates) and, for the vertical cross sections, the resolution of the analysis grids employed. As shown in Table 1, we recorded PPI scans at an angular resolution of one ray of data per degree of azimuth. We recorded each vertical or RHI scan at two different rates, a slower rate corresponding to a ray every 0.2° below 7.5° elevation to provide higher resolution near the surface, and the normal rate of one ray per degree above 7.5°. For reference, at a range of 8 km, the 1° angular resolution represents a spatial resolution of 140 m, and 0.2° angular resolution represents 28 m.

For this study we then transformed RHI scan data from the polar coordinates (range and elevation angle) of the original lidar data into Cartesian coordinates for analysis and presentation. For each vertical cross section we used two analysis grids: a 100-m horizontal by 25-m vertical grid up to 1.5 km AGL to study the details of the flow structure, and a 100-m by 100-m grid up to 4 km to look for flow layers, especially return-flow layers, through a deeper region of the lower troposphere. Lidar data were often not available much above 4 km because of the low concentrations of aerosols in the middle and upper troposphere, although smoke from Oregon forest fires improved the range and height of the lidar signal early in the project (Intrieri et al. 1990). The interpolation necessarily produced some smoothing of the data, and the Cartesian data were further filtered to provide smooth analyzed fields.

In the east–west cross sections presented in this paper, u_r to the west of the lidar was multiplied by -1 to produce an estimate of the westerly wind component u. From this two-dimensional u field we calculated the divergence of u, and then w from continuity using the procedures described by Mohr and Miller (1983) and Mohr et al. (1986). From the two-dimensional fields of u and w we made vector plots of the flow near the coast. An example of this kind of plot is presented in section 4 (Figs. 6–7).

b. Other instrumentation

Other instrumentation deployed during LASBEX included surface stations, radiosondes, and Doppler sodars. Intrieri et al. (1990) discuss these systems, and a brief description is also given in the Appendix.

c. Locale and meteorology

1) TOPOGRAPHY

The terrain immediately east of Monterey Bay is rolling farmland where most of the nation's artichokes are grown. The local wind systems in this region were of course strongly affected by the diurnal land–sea temperature contrast that drives the sea and land

breezes. Several mountain ranges in the area, though, also strongly influenced the local winds (Fig. 1b). To the north and northeast are the Santa Cruz Mountains, and to the east and southeast, the Gabilan Range. A gap between these ranges lies ~25 km east of Monterey Bay, but another ~30 km east of this gap the extensive Diablo Range stretches along the western boundary of the San Joaquin Valley, where summer and early fall temperatures often exceed 40°C. South of the bay are the Sierra de Salinas and Santa Lucia Mountains.

Extending southeast from Monterey Bay is an important feature for this study, the Salinas River valley. This valley, lying between the Gabilan Range to the east and the Sierra de Salinas to the west, is about 20 km wide at its mouth and extends ~140 km to the southeast at an orientation of ~140° from north. Flow from this direction observed by the lidar during morning hours often represented a continuation of nighttime down-valley flow.

More locally, a sand dune to the west of the lidar prevented the lidar from scanning all the way down to 0.0° elevation; the minimum elevation in this direction was ~0.1°.

On a larger scale the coastal mountain ranges of California are important because they keep the cooler marine air from penetrating eastward into the arid interior valleys of California (Fosberg and Schroeder 1966; Schroeder et al. 1967). As a result these inland regions become very warm. This produces a very strong low-level temperature contrast between the ocean and the continent on a scale even larger than that of the Monterey Bay sea breeze.

The central meridian for the Pacific time zone (120°W) passes less than 2° east of the LASBEX study area. Thus, at the equinox (22 September) sunrise was very close to 0600 and sunset was at 1800 Pacific Standard Time (PST). These local times corresponded to 1400 and 0200 UTC. California was on daylight savings time, so "local" times recorded during the project were 1 h later than PST. Times used in this paper are UTC.

2) SYNOPTIC CONDITIONS

The typical warm-season surface pressure pattern over the California coast was evident on many days during LASBEX. This pattern consisted of a subtropical high over the ocean and a thermal trough inland, resulting from the strong heating there. A surface chart given by Johnson and O'Brien (1973, see their Fig. 4) shows this pattern. Upwelling of cold subsurface ocean water maintains cold surface waters off the coast (Johnson and O'Brien 1973). The strong thermal gradient between the cold water and the hot interior valleys reinforces the synoptic pressure pattern.

Geostrophic balance dictates northerly or north-northwesterly flow along the coast. Frictionally induced, cross-isobaric flow near the surface produces an onshore flow at low levels. This is the flow that Fosberg and Schroeder (1966) and Schroeder et al. (1967) referred to as a "monsoon." The diurnal sea breeze, they assert, is "superimposed on the monsoon flow" (Fosberg and Schroeder 1966, p. 575).

In late September storm tracks started to dip farther south below the Canadian–United States border. On two occasions during the project, 15 and 26 September, cold fronts had pushed through Washington and had left a cool high pressure center over central Idaho. As the cold fronts moved southward past Monterey Bay on these days, the low-level flow at a height between 0.5 and 1.5 km turned easterly (offshore). Backing of the winds with height (from northeast to north) below 3 km indicated cold advection through the layer. This pattern thus interrupted the basic summertime onshore flow pattern, usually for a period of 2 or 3 days, and reversed the low-level ambient flow to offshore. Fosberg and Schroeder (1966) presented a case study of this kind of day, and their Fig. 29 shows a surface chart of this pattern.

In this paper we present surface mesonet data from both types of day as well as days with intermediate characteristics. The lidar case studies, however, address only the second type of day, that is, days with ambient, low-level offshore flow, since the sea breeze is easier to determine under these conditions, because the transition is distinct. Thus, this study does not emphasize the normal summertime regime.

3) THREE TYPES OF TRANSITION

During the two weeks of LASBEX we took data under a variety of meteorological conditions. To appreciate the variability of the timing, intensity, and structure of some of the features we observed, and to help us focus and interpret the large amount of lidar data that we took, we analyzed data from conventional instruments. We identified three types of transition from land to sea breeze by studying time records of surface station data from the triangle southeast of the lidar. We identify the transitions as abrupt, gradual, or in between as illustrated in Fig. 2.

Analysis of upper-air data likewise indicated three regimes. The "ambient" flow in this study refers to the larger-scale (synoptic or mesoα scale) flow at some level above the surface (generally observed between 0.5 and 1.5 km AGL) into which the developing sea or land breeze grew. The ambient flow determinations for each of the days of lidar operation are given in Table 2. The table also shows the correspondence between the ambient flow regime and the type of transition as determined by the surface station data. Abrupt transitions occurred with an easterly (offshore) component to the ambient flow, and gradual transitions occurred with westerly (onshore) ambient flow. This relationship is consistent with the findings of Estoque's (1961) numerical modeling study.

3. Offshore flow days

Offshore flow days with abrupt sea-breeze frontal transitions offer the best view of the change from land

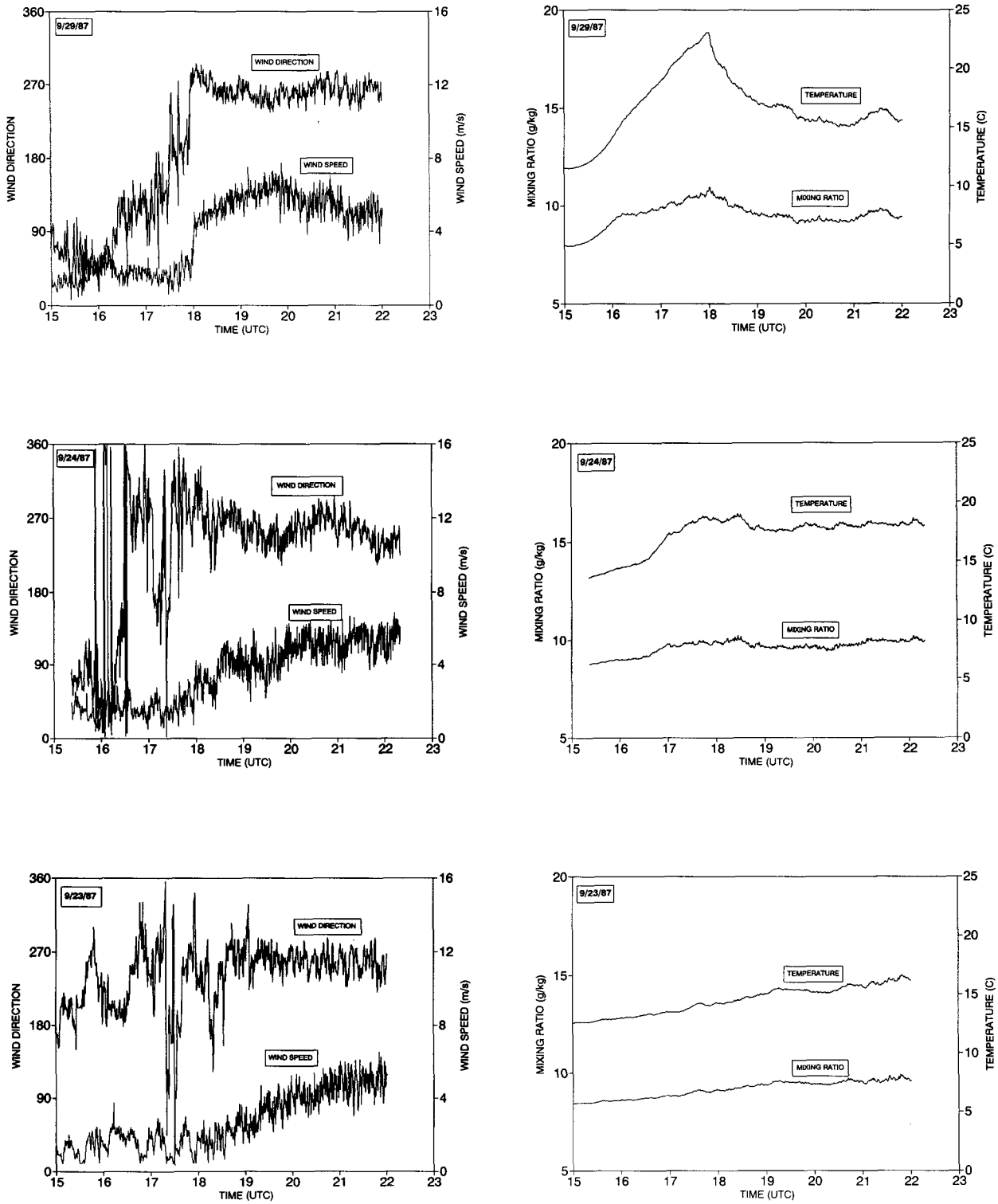

FIG. 2. Surface station traces of temperature, mixing ratio, wind direction, and wind speed at the primary sodar site for the three types of day observed during LASBEX. The top pair is for an abrupt day (29 September). The sharp drop in temperature, sudden increase in wind speed, and the shift from land breeze to sea breeze are evident. The bottom pair (23 September) is for a gradual day. Such days did not have a sharp change in temperature, and the wind speed increased more gradually. The middle pair (24 September) is for an in-between day. The wind shift, increase in wind speed, and drop in temperature are not as abrupt as during the offshore days, but more well defined than during the gradual days.

TABLE 2. Ambient wind directions for days with the three types of sea-breeze transition.

Abrupt		In between		Gradual	
Day	Direction	Day	Direction	Day	Direction
16	E	15	N	22	NW
21	NE	18	S	23	W
26	NE	24	NW	25	W
27	NE	28	NW		
29	E				

breeze to sea breeze using lidar measurements, because the direction of the early sea-breeze flow is opposite to that of the ambient flow. Two of the five days during LASBEX that had offshore (easterly) ambient flow and an abrupt sea-breeze front had good lidar data (Table 2). These days (16 and 27 September) had morning fog that cleared and therefore did not interfere with obtaining good lidar data. The lidar was able to measure u_r from early morning to afternoon, including the transition from offshore flow to sea breeze. In the following two subsections we analyze data from these days in detail.

On two other of the five days (21 and 26 September) fog prevented the lidar from observing the morning flow over the sea, but we did obtain data on the early sea breeze over land. After the fog lifted, the lidar measured the developing and mature sea breeze over both land and water. We analyzed the data from these incomplete-dataset days, even though some data are missing during the times of greatest interest. We refer to information from these days qualitatively in this paper, and we also include quantitative data on the dimensions of the sea-breeze layer in section 4c (Fig. 17 and Table 3). Finally, 29 September was too foggy and cloudy to obtain good measurements at any stage of the sea breeze. The small amount of lidar data taken on this day is not discussed in the present study.

a. 27 September 1987

1) HORIZONTAL STRUCTURE

Figure 3 shows the horizontal evolution from ambient offshore flow to sea breeze on 27 September. The top four panels show the demise of the offshore flow and the beginnings of the sea breeze near the coast. At 1632–1640 UTC (0832–0840 PST, Figs. 3a and 3b) offshore winds blew from the southeast. Figure 3b, taken at a higher elevation angle than Fig. 3a, shows that the southeasterly flow is confined to ranges of 5 km or less, corresponding to a depth of 436 m. Easterly offshore flow is discernible in the higher-level winds (i.e., the winds at greater ranges). By 1701 UTC (0901 PST, Fig. 3c) the velocities close to the shore decreased from >8 m s^{-1} to 3 m s^{-1}. At 1759 UTC (0959 PST, Fig. 3d) a small area of light, westerly flow—the incipient sea breeze—is seen at the shore. The speed of the offshore flow decreased not only at the shore, but over the entire area (Figs. 3c and 3d).

The bottom two panels show the establishment of a mature sea breeze. From modest beginnings in Fig. 3d, the sea breeze grew in extent by 1903 UTC (1103 PST, Fig. 3e), especially to the east over land. At 2029 UTC (1229 PST, Fig. 3f) a well-developed sea breeze, with velocities up to 9 m s^{-1} at the shore and greater over water, is shown. The last two scans also show that the sea breeze was two-dimensional and normal to the coast at low levels inside the first (5 km) range ring; the zero radial velocity line is nearly parallel to the coast (i.e., north–south) and the speed maximum is due west.

The horizontal variability exhibited in several of the scans in Fig. 3 demonstrates effects of terrain on the sea breeze. Figure 3 shows the effect of the Salinas River valley, to the southeast of the lidar, on the transition from offshore flow to sea breeze on 27 September. The offshore flow at 1632–1640 UTC (Figs. 3a and 3b) was strongest to the southeast, a combined result of the wind being channeled by the valley and the land breeze being augmented by the down-valley breeze, with cooler, denser air flowing down the Salinas Valley. By 1701 UTC (Fig. 3c) two flows are seen inland of the lidar: to the east, the final stages of the offshore flow were within 5 km of the lidar, and to the southeast, the down-valley flow was visible out to distances greater than 15 km from the lidar. At 1759 UTC (Fig. 3d) the sea breeze had just begun near the coast, but flow toward the lidar still persisted from the direction of the Salinas Valley (and from the north). Over the land to the east, westerly (onshore) flow extended beyond the edge of the figure, more than 12 km inland, most likely resulting from the beginnings of daytime upslope winds blowing toward the mountain ranges to the east (see Fig. 1b).

By 2029 UTC (Fig. 3f) a well-developed sea breeze existed, and terrain effects were less evident. Daytime instability and vertical mixing over the land produced sea-breeze flow that was horizontally more uniform than earlier in the day. A tendency for the westerly flow to be deflected to a northwesterly flow up the Salinas Valley as it passed over and to the southeast of the lidar could still be detected during the afternoon hours. This tendency was observed on other days.

2) VERTICAL STRUCTURE

Vertical cross sections from 27 September show the evolution from a different perspective. RHI scans, taken perpendicular to the coastline (i.e., parallel to the land and sea breezes), show the vertical and horizontal growth of the sea-breeze layer. The westerly wind component u in these east–west cross sections indicates the onshore component of the flow.

Figures 4–7 show a series of two-dimensional contour and vector plots of wind velocities from RHI scans taken on 27 September from the surface to 1.5

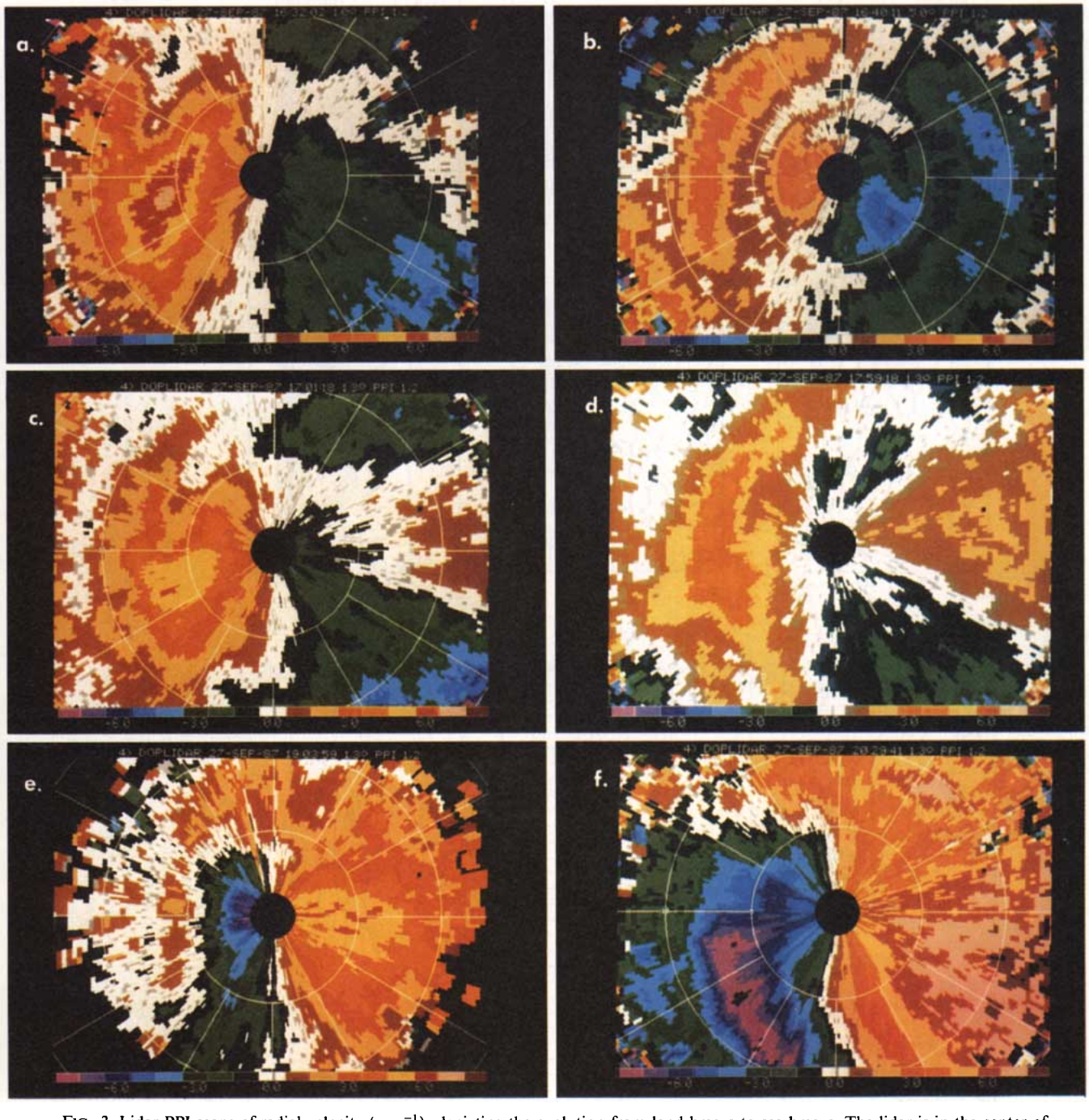

FIG. 3. Lidar PPI scans of radial velocity (m s^{-1}), depicting the evolution from land breeze to sea breeze. The lidar is in the center of each scan, and the indicated minimum range is 1.5 km. North is to the top, Monterey Bay to the left (west), and land (east) to the right. Range rings are 5 km apart and azimuth rays are every 30°. Negative velocities, represented by purple, blue, and green colors indicate flow toward the lidar. Positive velocities (tan, yellow, red) indicate flow away from the lidar. The time and elevation angle of each scan is as follows: (a) 1632:02 UTC, 1.0°; (b) 1640:11 UTC, 5°; (c) 1701:18 UTC, 1.3°; (d) 1759:18 UTC, 1.3°; (e) 1903:59 UTC, 1.3°; (f) 2029:41 UTC 1.3°. At 1.3° elevation, the 5-km range ring is at a height of 436 m and the 10-km range ring is at a height of 872 m.

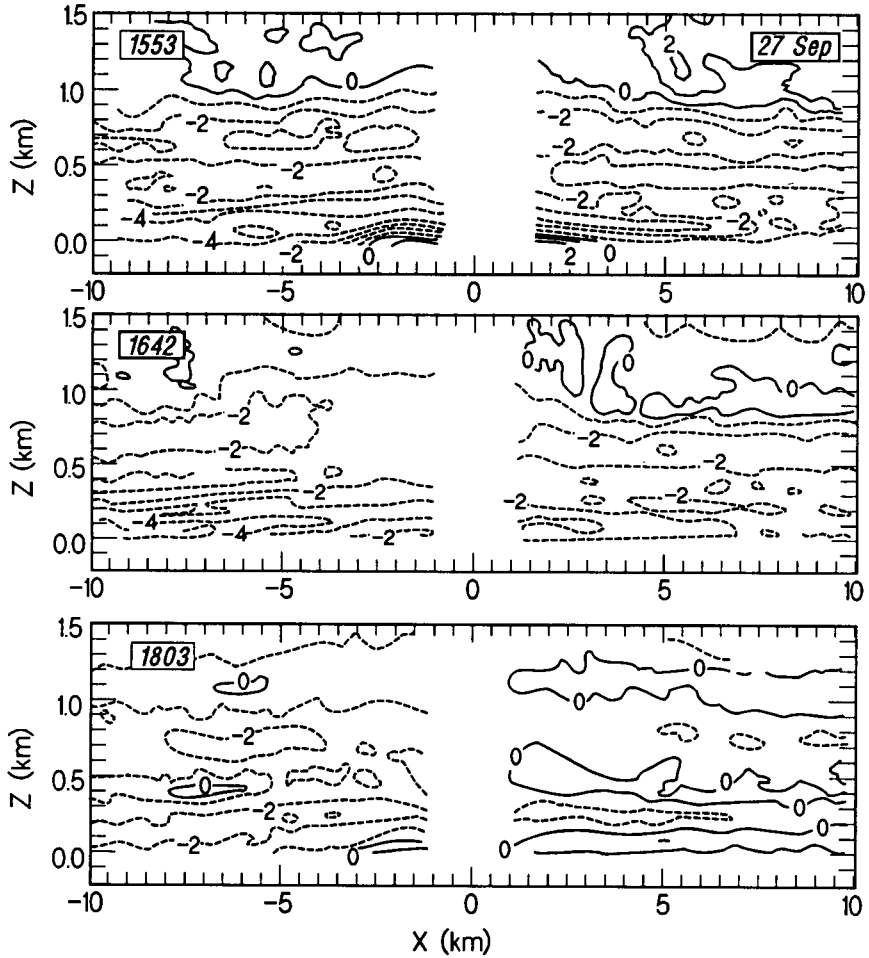

FIG. 4. Vertical cross sections of the u component of the wind on 27 September. The lidar is positioned at (0, 0), 1.5 km east of the shore. Monterey Bay is to the left, land to the right. Dashed lines indicate easterly flow and solid lines indicate westerly flow. Time (UTC) of the plot is in the upper left-hand corner. (a) Offshore flow of 1-km depth at 1553 UTC (0753 PST) with a "minor sea breeze" at the surface, near the shore. (b) Offshore flow at 1642 UTC (0842 PST). (c) Light westerly flow at the surface (sea breeze) underlying weakening offshore flow at 1803 UTC (1003 PST). Grid spacing was 100 m in the horizontal and 25 m in the vertical.

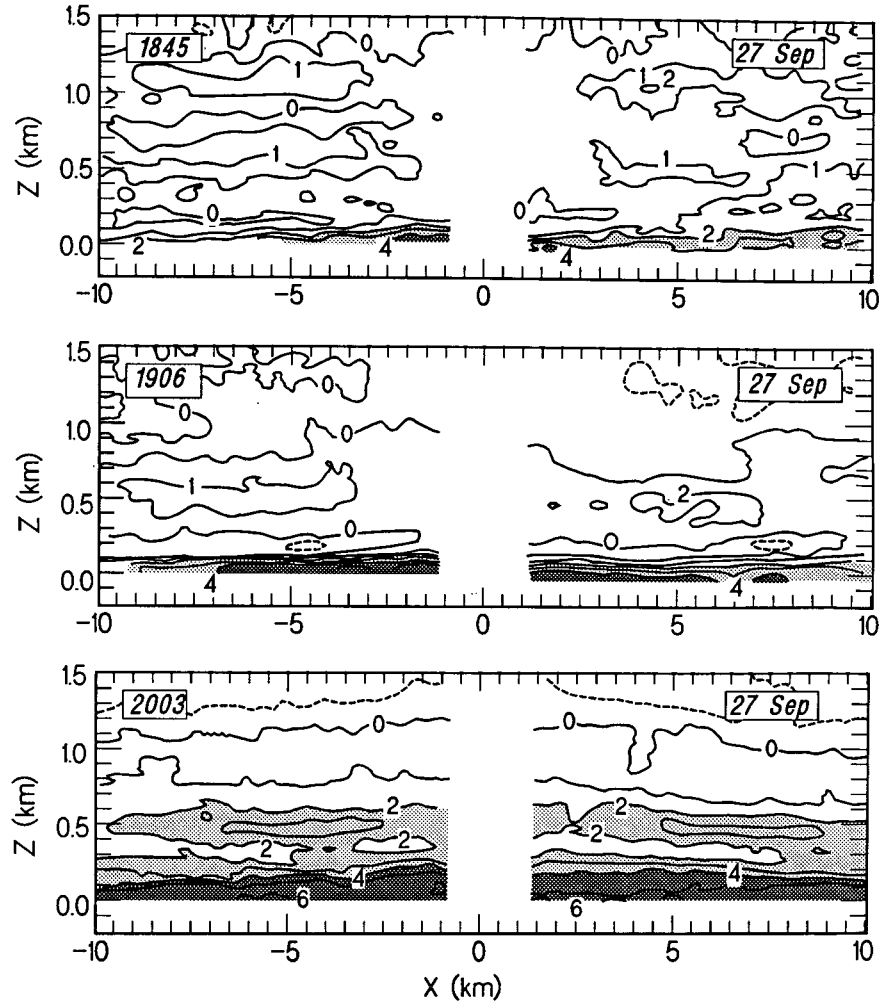

FIG. 5. As in Fig. 4, starting 42 min after Fig. 4c. The westerly, sea-breeze flow now extended up to 1.5 km, with the strongest winds near the surface. The sea breeze steadily increased in speed and became more well defined with time as illustrated at (a) 1845 UTC (1045 PST), (b) 1906 UTC (1106 PST), and (c) 2003 UTC (1203 PST). Light shading indicates flow over 2 m s^{-1}; dark shading, over 4 m s^{-1}.

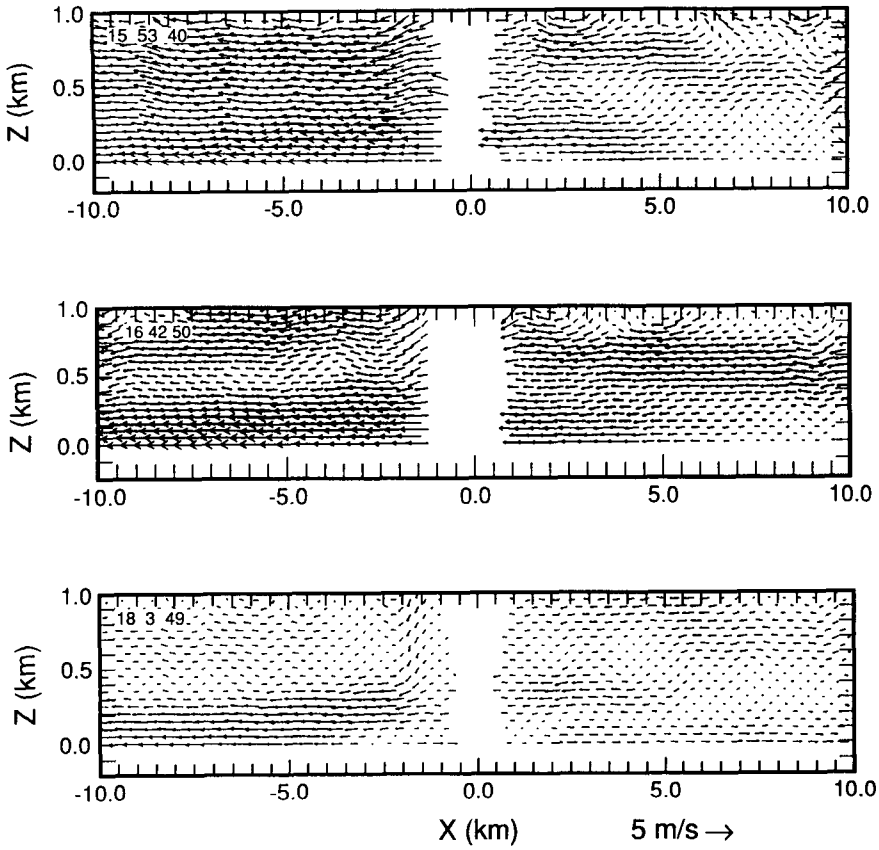

FIG. 6. Vector plots of the u and w components of the wind from the same scans seen in Fig. 4.

km. Figures 4a and 4b show the postfrontal offshore gradient flow reaching a height of ~1 km. An interesting feature of Fig. 4a (1553 UTC) is the small area of westerly flow near the surface at the shore. This early westerly (onshore) flow beneath the offshore flow appeared and then disappeared (Fig. 4b) before the steady sea breeze began. In the data from surface stations at the lidar and at the primary sodar site, this very local event showed up as a shift to light northwesterly (2 m s^{-1} or less) flow at ~1500 UTC, lasting for just less than 1 h. The transient sea-breeze precursor resembles the "minor sea breeze" of Conrad (1928), cited in Defant's review (1951). It is produced by the temperature contrast between the beach and the adjacent waters, and, as in this case, it precedes the normal or "major" sea breeze. In Fig. 4a the sea-breeze precursor circulation is 5½ km wide and a little less than 50 m deep. The cross section at 1642 UTC (Fig. 4b) indicates that this feature disappeared and the flow returned to the offshore flow from the surface to a height of ~1 km. The time and space extents of this minor sea-breeze phenomenon were thus very small.

By 1803 UTC (Fig. 4c) the offshore flow weakened considerably and a light, onshore flow, that is, the (major) sea breeze, began. The lidar-measured onshore flow coincided with a sea-breeze frontal passage at 1800 UTC measured by surface instruments at the lidar site (Shaw and Lind 1989). By 1845 and 1906 UTC (Figs. 5a and 5b) the offshore flow aloft continued to weaken, and the sea breeze increased in speed. By 2003 UTC (Fig. 5c) a mature sea breeze was established, extending upward at least 1 km from the surface.

The vector plots in Figs. 6 and 7 show wind vectors that are nearly horizontal at low levels, even at the edges of the circulations, indicating that w was small in the circulation. Calculated w values were less than 1 m s^{-1}. These values are smaller than values reported in many other studies of the sea breeze in offshore ambient flow, which were often 1–3 m s^{-1}. However, independent measurements of w taken by Doppler sodar over land during LASBEX showed that peak values for w at the passage of the sea-breeze front ranged from 0.2 to 1.0 m s^{-1} and averaged 0.56 m s^{-1} (Fagan 1988). The strong stability of the lower troposphere at the California coast undoubtedly contributed to these suppressed values for w.

The cross sections also show a strong asymmetry in the development of the sea breeze over land and water.

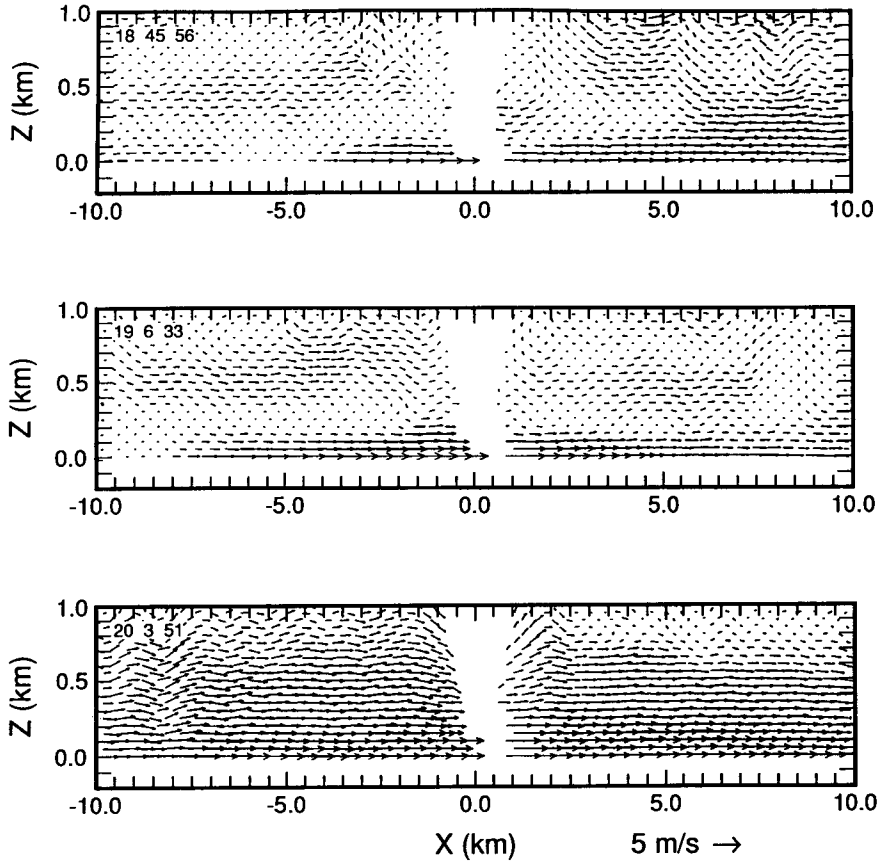

FIG. 7. Vector plots of the u and w components of the wind from the same scans seen in Fig. 5.

Over water the evolution was steady and well defined, but over land the sea breeze grew more quickly but was less well organized. The more turbulent growth of the onshore flow layer over land resulted from surface heating instability, but the more rapid development of westerly flow over land was more likely a slope flow effect. Upslope westerly flow toward the mountain ranges to the east apparently preceded the advent of the sea breeze near the coast and in other areas, as shown in Figs. 3c and 3d. The slope flow therefore aided in the landward growth of the Monterey Bay sea breeze (Mahrer and Pielke 1977).

3) EVOLUTION OF WIND AND THERMODYNAMIC PROFILES

A time sequence of vertical profiles of the horizontal winds on 27 September (Fig. 8) shows the evolution of the profiles over the lidar site. These profiles were determined by the lidar using the VAD procedures described in section 2. Easterly flow is evident up to 900 m until 1700 UTC, and a lidar 45° VAD wind profile (not shown) taken at 1600 UTC showed northerly flow between 1 and 3 km AGL, indicating cold advection concentrated between 900 m and 1 km. At 1800 UTC a shallow sea-breeze (westerly flow) layer appeared from the surface to 65 m, deepening to greater than 600 m by 1930 UTC. Figure 8 shows two other interesting characteristics: 1) The first indication of the transition to the sea breeze occurred aloft at 400–500 m between 1700 and 1730 UTC, when the westerly flow slowed and then deflected to a northerly direction. This occurred ½ to 1 h before the sea breeze began at the surface. 2) The offshore flow and the sea breeze were nearly easterly and westerly, respectively, and therefore one could use the westerly component of the wind (as in the east–west cross sections described in the previous section) to characterize the flow without losing significant information.

Two radiosonde ascents were made at the primary sodar site near Castroville: an early morning sounding at 1435 UTC and a midday sounding at 1936 UTC (Fig. 9). Both show a strong, capping stable layer, below 500 m on the earlier sounding and below 300 m on the later sounding. Temperature–dewpoint soundings (Shaw and Lind 1989) show that the 8 g kg^{-1} mixing ratio layer below 200 m in Fig. 9a is saturated, whereas the 9 g kg^{-1} layer below 300 m in Fig. 9b is not. Comparing Fig. 9b with the wind profiles at similar times in Fig. 8, it is apparent that the sea breeze extended upward to over 800 m, well into the stable layer that began at ~100 m AGL.

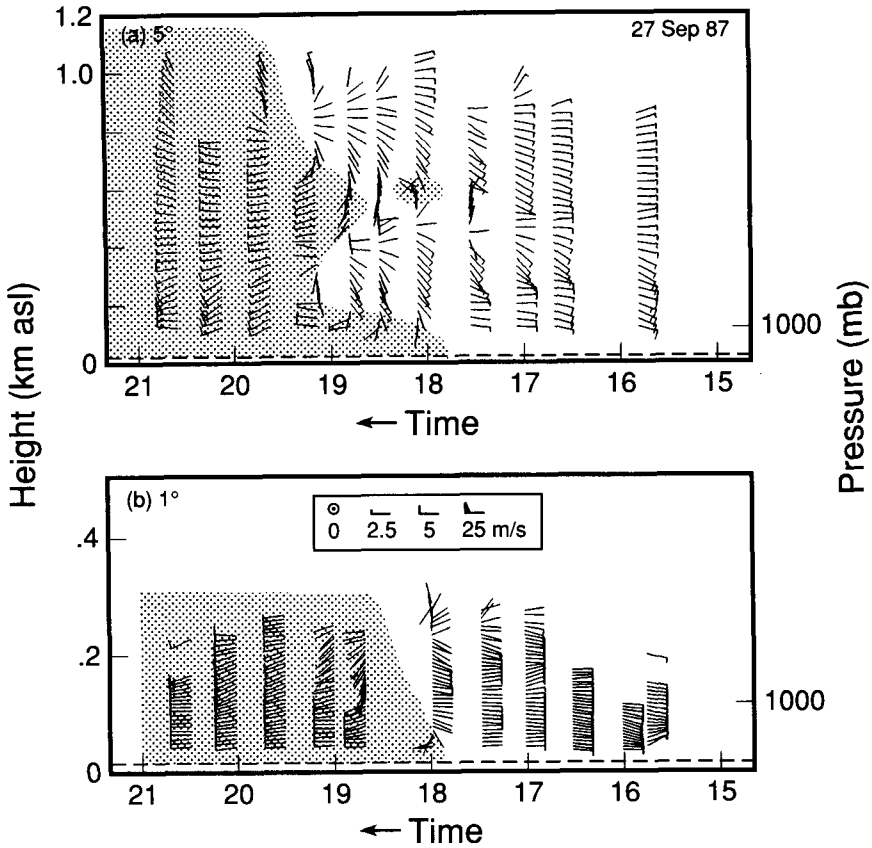

FIG. 8. Profiles of the horizontal wind on 27 September derived from conical (PPI) lidar scans using the VAD procedure. Time (UTC) is from right to left. Barbs pointing to the left symbolize westerly flow, barbs pointing to the top symbolize northerly flow. Westerly flow (sea breeze) is shaded. (a) Profiles from 5° PPIs. (b) Profiles from 1° PPIs.

b. 16 September 1987

1) VERTICAL STRUCTURE

The pattern of the vertical cross sections for 16 September was similar to that on 27 September, except that any minor sea breeze, if present, was less evident. Some pockets of westerly flow at the surface appeared in the morning prior to the major sea breeze, but these pockets were shallower, more disorganized, and more transient than the early, onshore precursor flow on 27 September. Thus they appear to have resulted more from turbulent processes than organized thermal contrasts between land and sea.

Figures 10 and 11 show contour plots similar to those in Figs. 4 and 5. Figure 10a shows postfrontal offshore flow extending to above 1.5 km, but the winds at the surface near the shore were very light in preparation for reversal to onshore flow. By 1713 UTC (0913 PST, Fig. 10b) a small area of shallow westerly flow began at the shore just to the west of the lidar. Farther out over the water the offshore flow was still strong, but near the surface over land it was weakening. At 1747 UTC (0947 PST, Fig. 10c) the total seaward-plus-landward extent of the sea-breeze layer was nearly 11 km, and the strength of the sea breeze exceeded 2 m s^{-1} at the coast. Surface station data indicated a frontal passage and wind shift at Moss Landing at 1645 (0845), and a shift to westerly flow at the primary (northern) sodar site between 1730 and 1800 (0930 and 1000 PST), consistent with the lidar cross sections. Figures 11a–b show the strengthening and deepening of the sea breeze from 1856 to 2026 (1056 to 1226 PST), and Fig. 11c at 2326 (1526 PST) shows a major change in the structure of the sea-breeze layer, as the wind-speed maximum, which had previously been at the surface, appeared aloft at ~200 m above the surface.

The vector plots (not shown) give a similar picture of the developing sea breeze. The small values of w and the asymmetry in the growth of the sea breeze over land and water that were observed in Fig. 6–7 are also evident in these vector plots.

2) EVOLUTION OF WIND AND THERMODYNAMIC PROFILES

Vertical profiles of the horizontal winds as a function of time are shown in Fig. 12. These are VAD profiles calculated from conical lidar scans at elevation angles

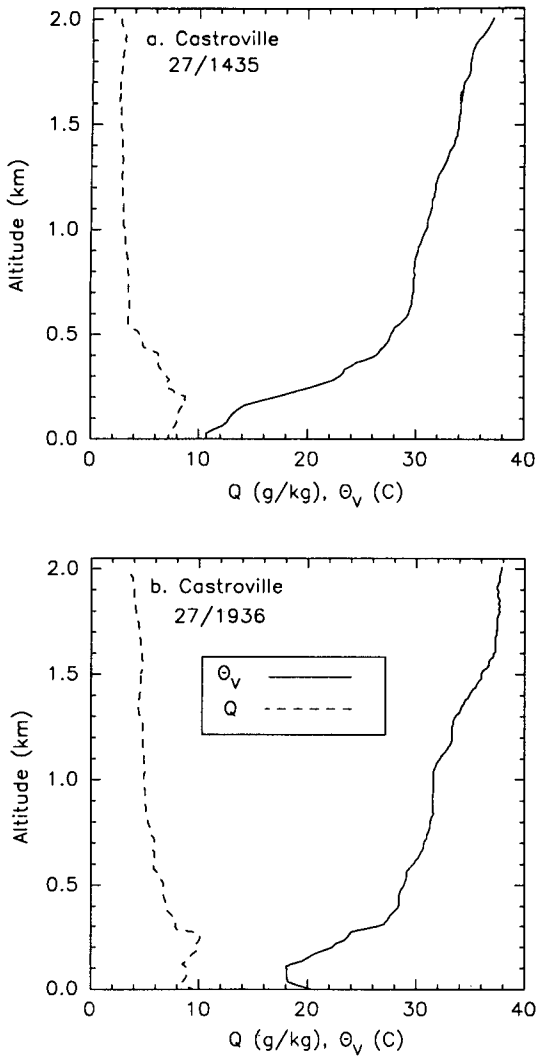

FIG. 9. Radiosonde ascents from the primary sodar site near Castroville, California, showing vertical profiles of virtual potential temperature (θ_v) and specific humidity (q) for 27 September: (a) 1435 UTC (0635 PST) sounding showing a stable, capping layer below 500 m. (b) 1936 UTC (1136 PST) sounding showing the stable layer below 300 m.

of 1°, 2°, and 5°. They show the sea-breeze layer starting at the surface at about 1720 UTC and growing slowly for the next 2½ h to about 250 m in depth. The reversal to westerly, sea-breeze flow above 250 m occurred only after 2000 UTC.

Radiosonde profiles of θ_v and mixing ratio taken from the *Silver Prince* (Figs. 13a–c) show a strong stable layer persisting below 300 m above the sea surface. The sounding at 2209 UTC (Fig. 13c) shows that a shallow mixed layer formed in the lower half of the inversion layer by late afternoon. A late-afternoon sounding over land at 2240 UTC (Fig. 13d) showed a deeper (400 m) but less sharp inversion layer at the primary sodar site and a deeper afternoon mixed layer than that over the ocean.

The wind profiles that accompany the last two *Silver Prince* soundings at midday (1957 UTC) and in mid-afternoon (2209 UTC) are given in Figs. 14a and 14b. Sea-breeze flow up to ~225 m during the earlier sounding, which was consistent with the 2026 (1226 PST) lidar cross section (Fig. 11b), was contained within the inversion layer, but in the later sounding the 850-m-deep sea-breeze layer, also consistent with lidar cross-section data, extended well above the 300-m-deep marine inversion.

4. Properties of the sea-breeze layer

a. Return flow

A precise definition of return flow is very difficult to find, especially one that allows for gradient flow. The concept of a return flow owes much to a model of the sea-breeze system as closed, in which ". . . a return [current] . . . aloft brings the warmer air back out to sea where it descends toward the sea surface to close the circulation" (Stull 1988, p. 593). A clue as to what is generally meant by return flow is the recurrent theme in descriptions of return flows, that the strength of the return flow is half that of the sea breeze, so therefore the depth of the return flow is twice that of the sea breeze—as "expected" or "required" by mass continuity (e.g., Atkinson 1981, p. 146). This implies that the amount of mass passing landward per unit time across the shore at low levels in the sea breeze equals the amount of mass passing seaward per unit time in the return-flow layer aloft. The return flow thus compensates for the landward flux of mass in the sea breeze. This definition of the return flow as a compensatory current is the one we refer to in this paper, noting first that a closed circulation is not *required* by this definition, and second, that the definition in practice will become more imprecise as the strength of the onshore or offshore gradient flow increases.

Convincing cases of compensatory return flows exist in the literature, especially under conditions of weak synoptic forcing and simple inland topography. For example, Lyons and Olsson (1973) showed return flow in the Chicago lake breeze using a combination of serial pibal ascents at three stations, tetroon flights, and smoke pollution observations. Lyons (1972) found that the return flow is such a recurrent feature of the Chicago lake breeze that he used its presence as a criterion for defining a lake-breeze event.

We searched vertical cross sections from the LASBEX dataset such as Figs. 4–7 and 10–11, similar cross sections that extended up to 4 km, and time plots of vertical wind profiles for evidence of compensatory return flows above the local sea-breeze layers. On some occasions, such as the morning of 16 September, an offshore flow layer aloft existed for ~3 h after the start of the sea breeze, but it was difficult to tell in individual cross sections whether this "return flow" was compensating for the sea breeze or was merely the persistence of the large-scale, postfrontal, offshore flow. Indeed, as

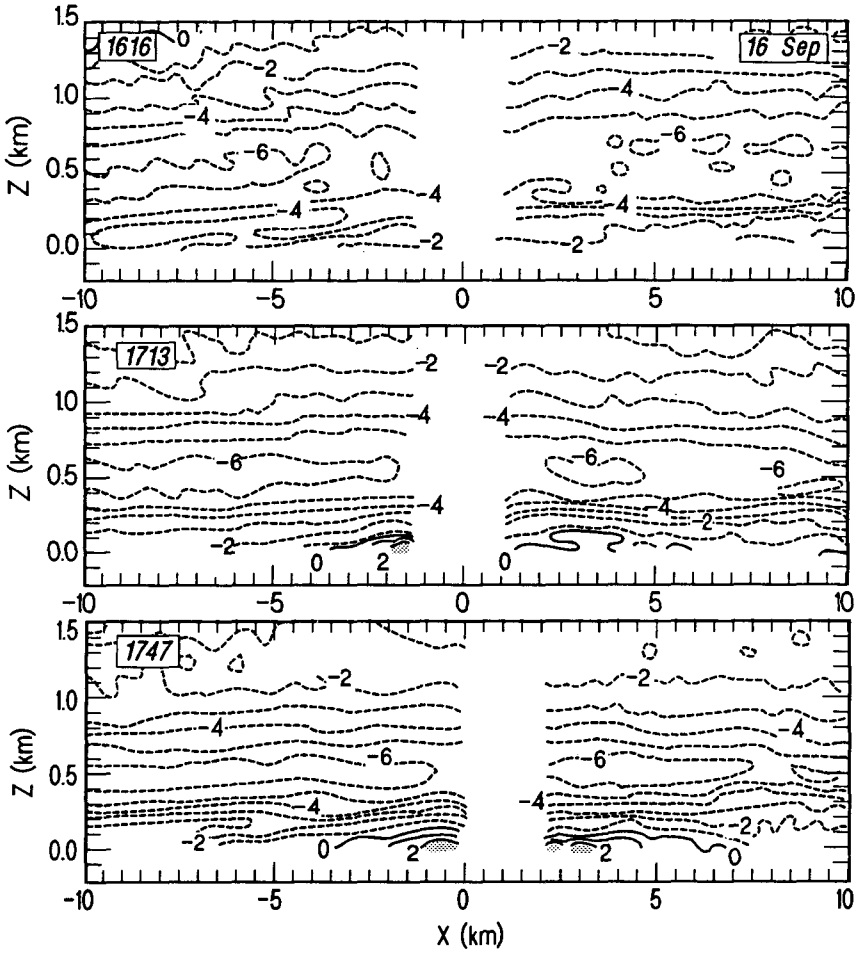

FIG. 10. Contour plots as in Fig. 4 except for 16 September. (a) Offshore flow regime at 1616 UTC (0816 PST) with an elevated layer of 6 m s^{-1} wind. (b) A new sea breeze at 1713 UTC (0913 PST) underlying a well-defined offshore flow. (c) The sea breeze continuing to develop at 1747 UTC (0947 PST) while the offshore flow stays intact aloft.

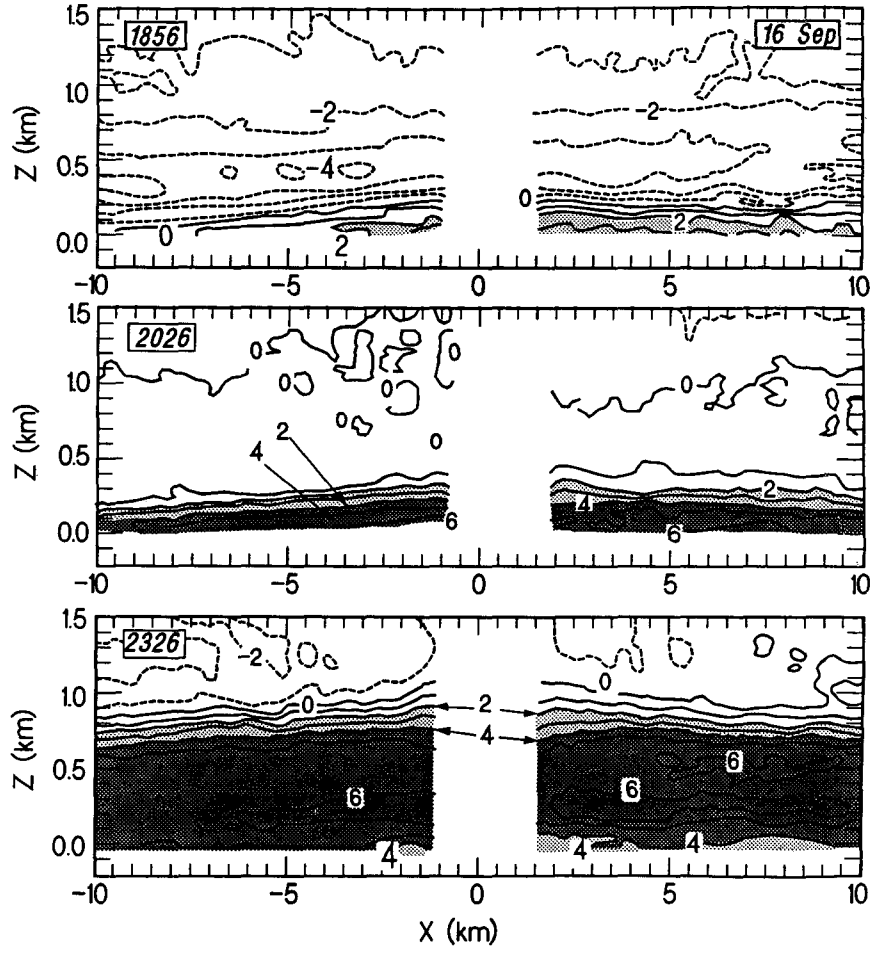

FIG. 11. As in Fig. 10, starting 69 min after Fig. 10c. (a) The offshore flow finally began to weaken by 1856 UTC (1056 PST). The sea breeze grew slightly in the vertical, but the horizontal growth was more extensive. (b) By 2026 UTC (1226 PST) the wind was westerly to ~1.5 km, with the strongest wind at the surface. (c) Mature sea breeze at 2326 UTC (1526 PST). Note that the strongest winds were no longer at the surface, but are a few hundred meters above the surface.

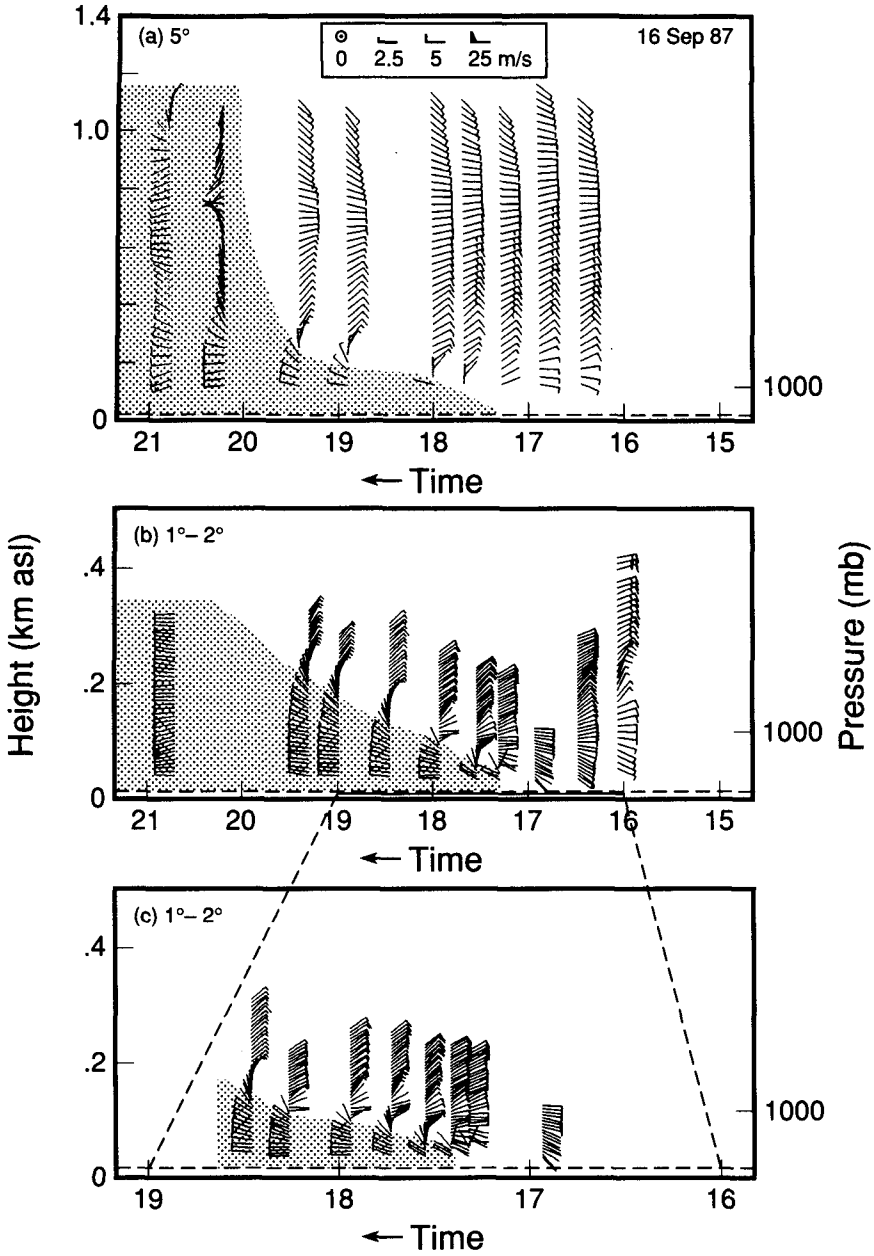

FIG. 12. As in Fig. 8 but for 16 September. (a) Profiles from 5° PPIs. (b) Profiles from 1° and 2° PPIs. (c) Additional 1° and 2° profiles for the time period 1600 to 1900 UTC.

the sea breeze blew stronger during the early afternoon, the offshore flow aloft grew weaker, implying that it was not a compensatory return flow. On other days, such as 27 September, there was no evidence in the data for a compensatory return flow above the local sea breeze. Reviewing both the 1½-km-deep and the 4-km-deep cross sections for all the days, we conclude that in general there is no consistent organized return-flow signal in the LASBEX dataset.

There are a number of possible reasons for the return flow to be absent in our analyses. 1) The return flow may be too small to detect, although it is difficult to imagine that a flow compensating for a sea breeze of 5 m s^{-1} or more would not be detectable. 2) The return flow may be distributed in the vertical in such a way as to be undetectable at any given level, but the strong stability of the atmosphere within 30 km of the shore suggests that compensation should be confined to lower levels in this region. 3) The return flow may be a perturbation superimposed on a stronger large-scale flow, but again, it should be detectable. 4) The return flow may not exist. This is the most convincing reason.

Near the surface the sea-breeze layer must be laterally bounded by a region of convergence (the sea-breeze

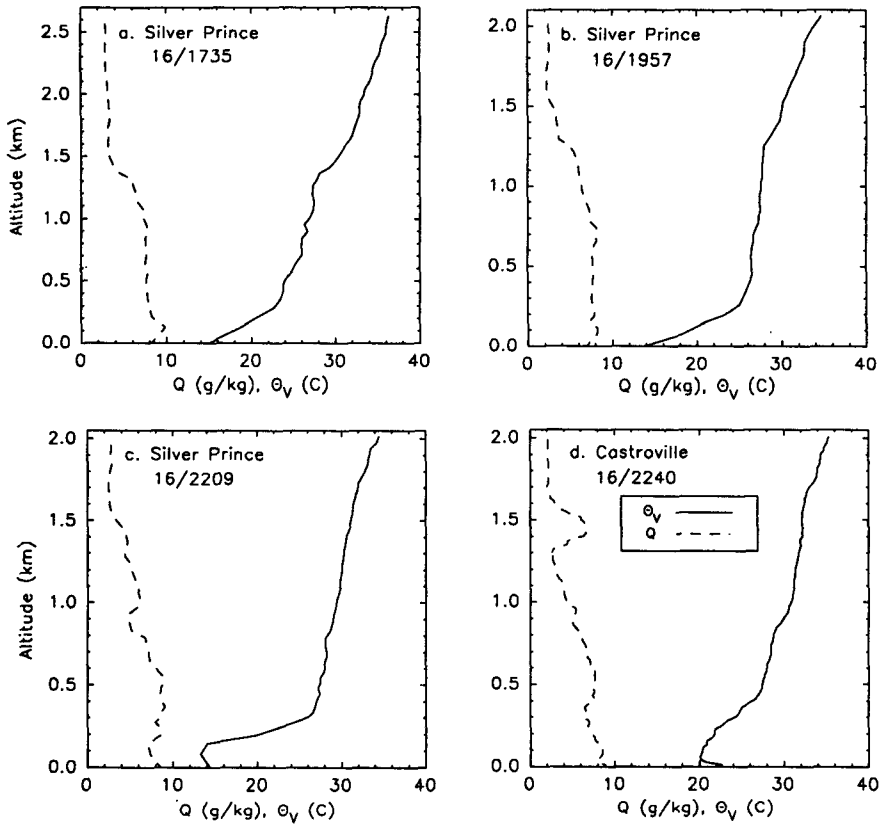

FIG. 13. Radiosonde ascents from the research vessel *Silver Prince* and from the primary sodar site, showing vertical profiles of virtual potential temperature (θ_v) and specific humidity (q) for 16 September. (a) A strong stable layer persisted below 300 m above the sea surface at 1735 UTC. (b) The same stable layer is observed at 1957 UTC. (c) A shallow mixed layer has formed in the lower half of the inversion layer by 2209 UTC. (d) At the primary sodar site at 2240 UTC, the inversion layer is deeper (400 m) but less sharp, and the late afternoon mixed layer was also deeper than over the ocean.

front) over land and divergence over water. The only requirements for mass continuity are that the convergence over land be compensated in a vertical column by divergence aloft (with a small residual left as a surface pressure change), and vice versa for the offshore divergence region. In an open system like the atmosphere, there is no requirement for the divergence above the onshore, sea-breeze convergence zone to be compensated locally by the offshore convergence aloft; that is, there is no *requirement* that the two regions be connected by a cross-shore return flow aloft.

At long coastlines where the inland topography is simple and homogeneous, where the larger-scale background flow is weak, and where the stability is weak so that strong vertical velocities can be generated, it is likely that the inland divergence or source of mass aloft would be compensated by the nearest strong sink or convergence region, which would be just offshore. In this case a return flow aloft (or a return perturbation flow) would most likely cross the shore. In LASBEX, however, the stability was strong and w's weak, and the onshore topography was very rugged. It is easy to envision the mass excess aloft, created over the land by the divergence above the sea-breeze front, being distributed over the land by being incorporated into slope or valley local wind systems, or by simply being absorbed into the deep inland convective boundary layer. Assuming that the mass entering the convergence aloft offshore were being supplied by offshore sources, no return flow across the shore would be required for mass continuity, since mass compensation is not local. Apparently this was the situation during LASBEX. Perhaps in general, compensating return flow aloft should be viewed as the exception under special circumstances, rather than the rule.

b. Time–height cross sections of the westerly wind component

We further analyzed the vertical cross sections of lidar wind data taken perpendicular to the shore (e.g., Figs. 4–5 and 10–11) to produce time–height cross sections of the westerly wind component u. At each vertical level we averaged the 21 points in the horizontal

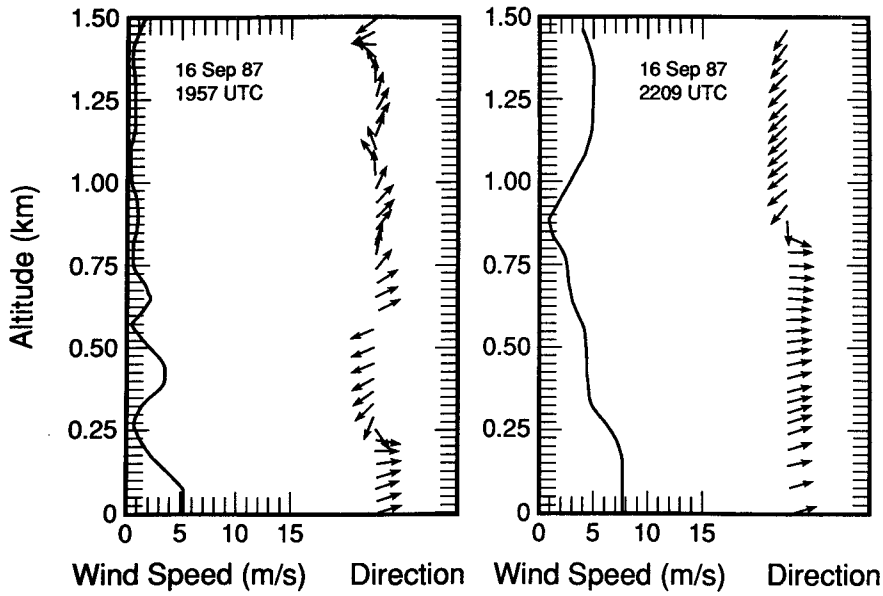

FIG. 14. Rawinsonde profiles of wind speed and direction (denoted by arrows) from the research vessel *Silver Prince* on 16 September. (a) The winds at 1957 UTC show that the sea-breeze layer is below 250 m in depth, and the wind has a 5 m s^{-1} maximum near the surface. (b) By 2209 UTC the sea-breeze layer has grown to approximately 850 m in depth, and a layer of 8 m s^{-1} winds has extended upward to 250 m (Shaw and Lind 1989).

between $x = -1$ and -3 km, which straddle the coastline at $x = -1.5$ km, to obtain profiles of u at the coastline. Time–height contour analyses are shown in Fig. 15.

Figure 15a shows the time–height cross section for 16 September based on 22 profiles between 1514 and 2326 UTC. The reversal from offshore flow to sea breeze began at the surface just before 1700 UTC, and the transition moved upward from the surface between 1700 and 2000 UTC. The offshore flow persisted in strength above 300 m until after 1800 UTC, when it diminished and eventually reversed to onshore flow at 2030 UTC. The notion that the sea breeze started at the surface is reinforced by the lidar VAD profiles in Fig. 12.

In contrast to the these profiles for 16 September, the VAD profiles for 27 September (Fig. 8) show the first indications of weakening offshore flow aloft at ~500 m above the surface and prior to the appearance of the sea breeze at the surface. The time–height cross section of u for 27 September, based on 12 profiles between 1553 and 2032 UTC (Fig. 15b), however, does not show this dramatic change aloft. The reason for the discrepancy is the difference in averaging procedure (the averages for Fig. 15 are along a 2-km horizontal line, whereas 5° VAD winds are averaged over a horizontal ring that has a diameter of >2 km at heights above 175 m). The cross section does show a hint of an acceleration in easterly offshore flow at 1730 UTC, indicated by closed contours of the -4 and -2 m s^{-1} isotachs. This increase interrupted a steady decrease in intensity of the offshore flow with time at all levels from the surface to 1.3 km. The decrease represented the transition from the strong offshore-flow profile that existed before 1600 UTC, as seen at the right edge of Fig. 15 (especially below 300 m).

In this case, therefore, (with weaker initial offshore flow between 400- and 1000-m height) the first indication of change occurred *aloft* between 400 and 500 m at 1700 UTC on Fig. 12. At the surface the reversal to onshore flow occurred at 1800 UTC. The distinction between the two days, one where the action started at the surface and the other where the action started aloft, may be important in determining how the sea breeze is initiated at the coastline.

Several reviews, including those of Defant (1951) and Atkinson (1981), qualitatively describe a sequence of processes by which a sea-breeze circulation begins; this sequence commences aloft. Surface heating just after sunrise causes the columns of air over land and water to heat and expand upward. This occurs more rapidly over land than over water. The surface-based expansion produces high pressure at some upper level over the land, and the high pressure produces a "slight flow of air from land to sea" aloft (Atkinson 1981). The resulting movement of air aloft results in a lowering of pressure at the ground over land, a rising of pressure offshore at the sea surface, and thus a pressure gradient that begins to drive an onshore flow, the sea breeze. According to this scenario, therefore, one expects a flow across the coastline (from the land to the sea) at some upper level, to precede the appearance of the sea breeze at the surface.

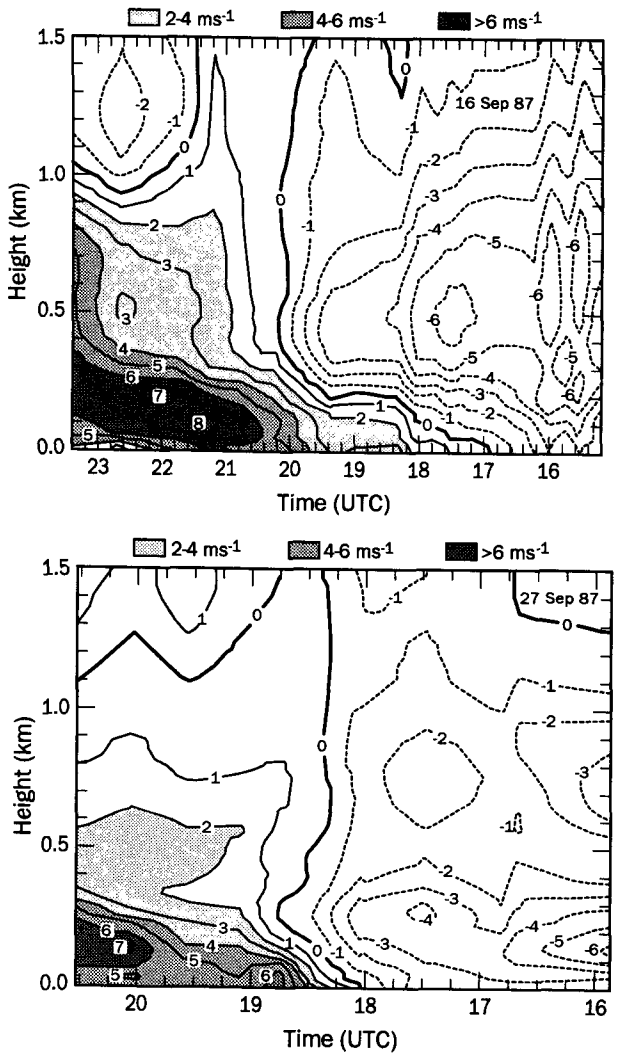

FIG. 15. Time–height cross sections of the u component of the wind. After lidar RHI scans were transformed from polar to Cartesian coordinates, profiles were obtained by averaging grid points 1 to 3 km west of the lidar and from the surface to 1.5 km. Time is from right to left. Dashed lines represent flow from the east, solid lines flow from the west. Westerly flow 2–4 m s^{-1} has light shading, flow from 4–6 m s^{-1} has medium shading, and flow greater than 6 m s^{-1} has dark shading. (a) Profiles from 16 September. The maximum speed of 8 m s^{-1} occurs just after 2100 UTC 50 to 100 m above the surface. (b) Profiles from 27 September. A brief maximum of 6 m s^{-1} occurs at the surface just before 1900 UTC, and an elevated maximum of 6–7 m s^{-1} flow can be seen starting at 2000 UTC.

Onshore flow data for 27 September (Fig. 15b) support this scenario only weakly, with a hint of seaward acceleration of flow between 250 and 300 m ~1/2 h before the surface reversal to sea-breeze flow. It would be reassuring to see this pattern in more than one case, but data for 16 September (Fig. 15a) show the sea breeze commencing at the surface, with no acceleration of the seaward flow aloft prior to the surface reversal. This behavior is shown in greater detail in Fig. 16a, which shows u as a function of time for several levels. The reversal to sea-breeze flow occurs first at the surface, but there is no increase in offshore flow aloft prior to the surface wind shift. Thus, the lidar-measured behavior of u on 16 September does not support the scenario described by Defant (1951) and Atkinson (1981) for the initiation of sea-breeze flow at the coastline, and the evidence from 27 September supports it weakly at best.

A problem with this scenario could be similar to the problem with the return flow described in the previous section. There can be little doubt that the preferential heating of the land surface and the atmosphere just above it must produce a stretching of the columns of air over land and relatively high pressure at some level aloft, compared with the same level over the sea. Divergence of mass (by advection, gravity waves, or acoustic waves) from the atmospheric column above (or within) the heated layer would produce a pressure drop at the surface, and this would initiate the sea breeze, perhaps simultaneously. The question is, how does this mass excess from the divergence aloft become redistributed? One way is for it to flow back over the coast, toward the sea, as suggested in the previously proposed scenario. Apparently on 16 September this did not happen, and the divergence of mass aloft must have been redistributed inland.

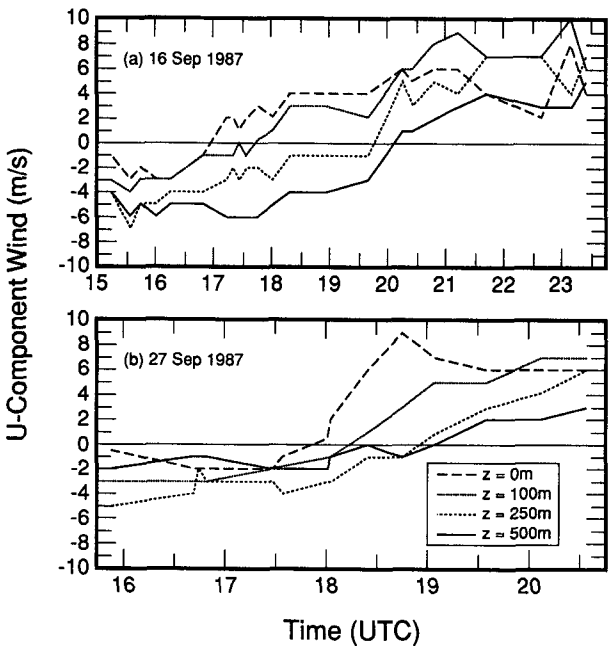

FIG. 16. The u component of the wind 1.5 km west of the lidar as a function of time at the surface, 100 m, 250 m, and 500 m for 16 and 27 September. (a) The growth of the sea-breeze layer on 16 September can clearly be seen occurring first at the surface, and then at the subsequent levels, with no increase in offshore flow aloft prior to the surface wind shift. (b) On 27 September the progression was similar with the sea breeze first occurring at the surface. Numbers were obtained from digital printouts from the same Cartesian gridded data that were used in the cross sections in Figs. 4–7 and 10–11.

On 27 September, however, there was a small acceleration in offshore flow detected aloft, and this could be an indication that on some days the proposed scenario is observed. Resolution of this dilemma must await further study.

c. *Growth of the sea-breeze layer*

Because the lidar was able to scan over the surface of the water, we were able to obtain information about the seaward propagation of the edge of the sea-breeze circulation. Traditionally this information has been very difficult to acquire. Arritt (1989), who studied this aspect of the sea breeze numerically, remarks about the difficulty in measuring offshore extent and the resulting paucity of good observations. In the present study we used lidar data to determine the offshore extent of the sea breeze as a function of hour of the day (Fig. 17 and Table 3). The offshore extent of the sea breeze was defined as the westernmost point where onshore flow existed. If we take the data on 27 September as an example, the sea breeze moved from ~3 km west of the lidar at the second observation just after 1800 UTC to ~10 km west of the lidar at the last observation just after 1900 UTC. The sea breeze moved outward ~7 km, implying a mean propagation speed of 7 km h^{-1} or 2 m s^{-1}.

We also obtained the depth of the sea-breeze flow (Table 3). Comparing these depths with the θ_v profiles (Figs. 9 and 13) one can see that as the sea-breeze layer deepened during the afternoon, it extended upward into the stable inversion layer. In contrast, Johnson and O'Brien (1973) found that the Oregon sea breeze was confined to the region below the inversion.

With the extent and depth of the onshore flow, we were able to calculate an aspect ratio of the horizontal to vertical dimensions for half of the sea-breeze circulation. Complications with the slope and valley flows and convective turbulence that were present over land often made it difficult to identify the extent of the sea breeze there, or at least made its behavior more erratic.

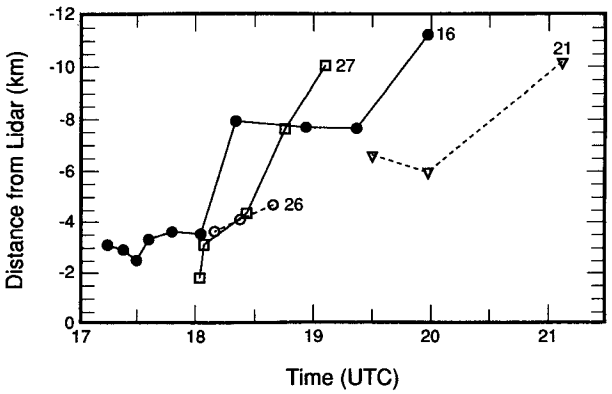

FIG. 17. Offshore extent of sea-breeze circulation as a function of time for 16, 21, 26, and 27 September. This was defined as the westernmost point where onshore flow existed. As in the previous figure, numbers were obtained from digital printouts from the same Cartesian gridded data that were used in the cross sections in Figs. 4–7 and 10–11.

TABLE 3. Dimensions and aspect ratios of the seaward branch of the sea-breeze layer: $L/2$ denotes the offshore extent of the sea breeze, and $H/2$ indicates the height of the onshore-flow layer. An asterisk indicates cross sections that exhibit two layers of onshore flow, a shallow and a deep layer, and SP indicates data based on the *Silver Prince* rawinsonde.

TIME (UTC)	$L/2$ (km)	$H/2$ (m)	L/H
	16 September 87		
1713	1.6	50	32.0
1721	1.4	75	18.7
1727	1.0	75	13.3
1735	1.8	75	24.0
1747	2.1	100	21.0
1802	2.0	125	16.0
1820	6.4	225	28.4
1856	6.1	225	27.1
1922	6.1	200	30.5
1959 (SP)	>11.2	225	>50.0
2017	>11.2	300	
2026*	>11.2	260	
2049*	>11.2	275	
2113*	>11.2	250	
2143*	>11.2	900, 250	
2209 (SP)	>11.2	850	
2239	>11.2	775	
2326	>11.2	900	
	17 September 87		
0112	>10.0	925	
0208	>10.0	1025	
0246	>10.0	1150	
0310	>10.0	875	
	21 September 87		
1930	5.0	200	25.0
1959	4.3	175	24.6
2107	>10.0	185	>54.0
2133*	>10.0	1100, 250	
	26 September 87		
1808	2.1	50	42.0
1821	2.6	100	26.0
1839	3.2	125	25.6
2017	>10.0	520	>19.2
2100	>10.0	400	
2150*	>10.0	1025, 425	
	27 September 87		
1801	0.3	25	12.0
1803	1.6	<25	>64.0
1826	2.9	150	19.3
1845	6.1	175	34.9
1906	>10.0	150	>66.7
1935	>10.0	200	
2003	>10.0	200	
2032*	>10.0	975, 300	

Therefore, we used the horizontal extent of the offshore half of the circulation (designated $L/2$), which was better behaved, as shown in the cross sections in Figs. 4–7 and 10–11. Because the upper, return-flow half of the circulation was generally absent, as discussed in section 4c, we used only the lower, sea-breeze "half" of the circulation (designated $H/2$), noting, however, that when return flows have been observed and modeled, they are often 2–3 times the depth of the sea-breeze layer. Thus, this dimension probably represents *less* than half of the actual depth of the entire sea-breeze circulation. If we accept this limitation, the resulting aspect ratio ($[L/2]/[H/2] = L/H$), representing half of the horizontal and half the vertical dimensions of the circulation, should be a reasonable estimate of the value for the hypothetical total circulation.

Table 3 gives the values of these dimensions and the aspect ratio for each east–west cross section taken on the study days. Two of the later entries for 16 September were provided by rawinsonde ascents from the *Silver Prince,* positioned 11.2 km west and 0.2 km south of Moss Landing, at 1959 and 2209 UTC, and shown in Fig. 14. For the days listed in Table 3, the aspect ratios tended to be between 15 and 25 for those observations after the sea breeze was greater than 50 m deep but before ~2000 UTC. The first observations of the sea breeze had aspect ratios that were larger, probably in part because the 25-m analysis mesh does not adequately resolve the layer, and observations after 2000 UTC are often affected by the presence of the larger-scale, regional sea breeze. The starred data in Table 3 indicate cross sections that have evidence of a deeper, regional-scale sea breeze developing.

It is of interest to compare the estimates of aspect ratio in Table 3 with aspect ratios predicted by some recent analytical models. Arritt (1989) pointed out that the quantity $N(f^2 - \omega^2)^{-1/2}$ in Rotunno's (1983) study can be interpreted as an aspect ratio L/H, where N is the Brunt–Väisälä frequency, $\omega = 2\pi$ day^{-1} is the frequency of the earth's rotation, the Coriolis parameter f equals $2\omega \sin\phi$, and ϕ is the latitude, which for Moss Landing is ~36.8°N. In their extension of Rotunno's work, Dalu and Pielke (1989) defined an aspect ratio, the inverse of which is

$$L/H \approx N(f^2 + \lambda^2)^{-1/2},$$

where λ is a frictional time scale to which Dalu and Pielke assigned a "typical" value of 1.2ω. This expression is valid for the long-time solution of their case in which heating is started impulsively. If we use the latitude of Moss Landing and a standard atmosphere θ lapse rate of 3°C km^{-1}, for which $N \sim 0.01$ s^{-1}, the Rotunno expression yields an L/H value of 208, and the Dalu–Pielke expression yields 81. Thus, Dalu and Pielke's (1989) inclusion of a frictional component in the time scale of the sea breeze produces better agreement with the values in Table 3. Still, both of these values are considerably larger than the observed values. Increasing the stability to isothermal nearly doubles the values of L/H, producing even poorer agreement with the observations. Therefore, the strong stability of the lower atmosphere along the California coast is not the reason for the discrepancy. More likely, the theoretical values are simply not compatible with the observations, because complications such as inland topography and conditions leading to the lack of return flow in the observed sea breeze are not included in the formulation of the models.

d. *Role of Coriolis*

A final aspect of the evolution of the Monterey Bay sea breeze is the Coriolis effect on the direction of the sea-breeze flow through the day. A great many studies, theoretical, observational, and numerical, have found that the Coriolis force turns the winds significantly through the daytime hours. We inspected the low-angle, quasi-horizontal (PPI) scans taken through the morning and afternoon hours of the days with opposing ambient flow to look for tendencies for the sea breeze to veer to the north, which would indicate Coriolis influence. We found no consistent tendency for the sea-breeze flow to turn northerly through the afternoon hours. On individual, isolated days the well-developed sea breeze occasionally turned to the northwest or southwest in the afternoon, but most often the flow stayed westerly, as shown in the wind direction traces in Fig. 2. Using surface records from Moss Landing, Yetter (1990) actually found *backing* of the surface winds with time on three of the LASBEX days, and data presented by Shaw and Lind (1989) show that this lack of veering was true on most days of the project. Although this finding contradicts the many studies that have found Coriolis turning of the sea breeze, it agrees with the results of Johnson and O'Brien (1973), who found no Coriolis turning in the sea breeze at the Oregon coast. It is tempting to speculate that topographical constraints on the flow may thwart Coriolis effects. Our data over the ocean, however, show no Coriolis turning there either, indicating that topography probably is not a factor in suppressing the Coriolis influence. An alternative explanation is that the absence of recirculation by return flows means that in a Lagrangian sense, air parcels do not stay in the sea-breeze circulation for a significant fraction of a pendulum day, that is, long enough for the Coriolis force to act on them (Atkinson 1981).

5. Summary and conclusions

The Monterey Bay sea breeze formed regularly during late morning hours on days during September 1987 with weak synoptic forcing. In many respects it resembled the sea breeze observed in other coastal areas. For example, surface station and upper-air data revealed a sensitivity of sea-breeze structure to ambient wind direction. The behavior of the sea breeze and the sea-breeze front in opposing (offshore) ambient flow was

similar to that reported by other researchers: the temperature reached a sharp peak and the surface winds reversed suddenly at the passage of the sea-breeze front. In the present dataset offshore ambient flow days were identified by a cold advection signature, with winds backing from northeasterly to northerly with height between 0.5 and 1.5 km. In ambient onshore flow the temperature gradient was more diffuse and the transition to the thermally forced sea breeze more gradual.

The sea breeze at Monterey Bay during the study period was affected by a number of complicating factors, though. The terrain just inland from the coast is complex and mountainous. The coastal waters are cold for the latitude, producing a strong, stable inversion layer within the lowest few hundred meters above the surface. Superimposed on the local temperature gradient at the coastline is a much larger-scale temperature contrast between the cold ocean waters and the hot interior valleys of California. The diurnal variation of this contrast can produce a larger-scale flow system in which the local sea breeze is embedded. Finally, most study days had fog along the coast, and on some days the fog extended inland. The surface radiation budget was thus strongly influenced by the distribution of fog along the coast and inland.

Because of these complicating factors we observed a number of differences from studies in other areas. Values for vertical velocity w inland at the sea-breeze front were small (less than 1 m s^{-1}), as a result of the strong atmospheric static stability along the California coast. In other coastal regions values of 1–3 m s^{-1} are not uncommon for w at the front. We also observed no Coriolis effect on the direction of the sea-breeze flow. Winds tended to blow from the west with no noticeable tendency to veer to the north through the afternoon. East–west vertical cross sections of the westerly wind component u showed no consistent evidence for a compensatory return flow aloft from land to water in the LASBEX dataset. This coincidence of absence of return flow and absence of Coriolis deflection is consistent with Atkinson's (1981) argument that Coriolis turning is produced when air parcels are recycled for several hours within the sea-breeze circulation cell. Because the sea breeze has no return flow, there is no recycling and no Coriolis effect.

The scanning capability of WPL's pulsed Doppler lidar allowed two-dimensional fields of u to be measured in a vertical plane perpendicular to the coast and parallel to the sea and land breezes. The narrow beam of the lidar yielded measurements with high vertical resolutions (28 m at a range of 8 km) close to the land and sea surfaces. These finescale measurements showed many interesting features of the vertical structure of the sea-breeze layer and its evolution. On one of the two days analyzed in detail, the lidar data revealed a short-lived precursor of onshore flow, which appeared at the coastline and then disappeared before the advent of the "major" sea breeze ~2 h later in the morning. The wind shift from offshore flow to the sea breeze began at the shore within 100 m of the surface. On one of the days studied, the sea breeze began at the surface and moved upward, and on another, the first indications of change occurred at 400–500 m above the surface about 1/2 h before the surface wind reversal. Wind speeds gradually decreased as the offshore flow dissipated, then the winds reversed direction at the surface as a small onshore flow developed. The sea-breeze circulation extended landward and seaward from the shore and increased in depth over time. Lidar cross sections allowed us to observe the growth of the offshore extent and depth of the sea-breeze layer and to calculate a length-to-depth aspect ratio. These aspect ratios compared poorly with predictions from analytical models, probably because the many complicating effects along the Monterey Bay coastline were not included in the idealized model formulations.

The horizontal nonuniformity of the Doppler wind velocities u_r, as revealed by quasi-horizontal lidar scans, shows influences of topography on the developing sea breeze. We saw two major topographical effects: 1) The westerly, onshore flow grew faster over land than over water, apparently because the heated, west-facing slopes generated an upslope flow. The asymmetry in the growth of the depth of the sea-breeze layer, which grew faster over land than over water, may have also been due in part to the complex terrain inland from Monterey Bay. 2) As westerly sea-breeze flow was establishing itself over most of the region within 20 km or so of the coast, southeasterly, down-valley flow persisted for up to 1 h in the Salinas River valley because of the inertia of that along-valley flow system. In addition to these two effects, we also found that complex inland terrain may have contributed to the absence of a compensatory return flow from land to sea over the coast. We hypothesized that slope or valley circulations over the complex topography would absorb the mass divergence aloft, which existed above the low-level convergence at the sea-breeze front, so that it would not be necessary for this mass to flow back over the coastline; that is, it is not necessary for mass compensation to occur locally within the sea-breeze system.

This picture of the central California sea breeze was based mostly on data from WPL's Doppler lidar, and the lidar data were shown to be consistent with observations from other systems. The timing of the sea-breeze reversal as seen by the lidar agreed with observations from the surface stations, and the depth and strength of the sea breeze from lidar cross sections also agreed well with wind profiles over Monterey Bay. Moreover, the lidar results showed that the behavior of the sea-breeze layer was consistent with behavior expected of this kind of thermally forced flow from theoretical models, from numerical model results, and from other observational studies. The layer formed at the shore in the morning after several hours of heating, grew in width and depth, and dissipated at night. The agreements with observation and expected behavior give confidence in the lidar results. But the lidar also

found some unexpected behavior, such as the absence of return flow aloft. These unexpected results must also be accepted, because 1) the aerosol backscatter intensity was high in both layers and produced more than adequate signal-to-noise ratios for reliable velocity estimates, 2) the physics of calculating the speed of movement of objects (in this case windborne aerosol particles) from a Doppler shift using lidar is well established, 3) measurements of frequency are among the most reliable measurements one can make remotely, and 4) the measured speeds greatly exceeded the rms error of the lidar system of 60 cm s^{-1}.

The results of this study were obtained by combining remote sensing observations of Doppler lidar and sodar with conventional in situ measurements using surface meteorological stations and radiosonde instrumentation. From the lidar data we were able to discern layers and horizontal variability of the lidar-centered radial wind component. Surface station and rawinsonde observations showed the actual directions of winds and thus complement the lidar data. Surface station time series showed the nature of the sea-breeze front, allowing the large volume of lidar data to be stratified by type of sea-breeze front (abrupt, gradual, in between). The sodar provided direct measurements of w to compare with order-of-magnitude estimates based on lidar data. The instrumentation deployed during LASBEX thus gave us a much better picture of the Monterey Bay sea breeze than any of the instrumentation systems by themselves would have provided.

Acknowledgments. We thank Richard Cupp and the other members of the lidar group who operated and maintained the lidar during the field experiment. We also thank the following for their roles in organizing and operating LASBEX: Gordon Little, William Shaw, and Tak Cheung, and we thank our colleagues Janet Intrieri and William Shaw for helpful discussions of LASBEX and the Monterey Bay sea breeze, Zhu Cuijuan and Mark Vigneault for their help in data analysis and manuscript preparation, and Dominique Ruffieux for providing the map in Fig. 1b. Jim Wilczak, Tanniel Uttal, and Janet Intrieri provided helpful reviews of the manuscript, and Christine Sweet gave us many technical editing suggestions for improving the manuscript.

APPENDIX

LASBEX Instrumentation

a. Surface stations and radiosonde

Six mesonet stations were deployed for LASBEX. They provided temperature, humidity, atmospheric pressure, wind speed, and wind direction at 20-s intervals. Three of the stations, provided by the Naval Oceanic and Atmospheric Research Laboratory (NOARL) [formerly the Naval Environmental Prediction Research Facility (NEPRF)], took data at each of the vertices of the "sodar triangle" indicated on Fig. 1a. The other three systems were operated by the Naval Postgraduate School (NPS). One was redundantly located at the primary sodar site at the northernmost vertex of the sodar triangle, one was at the lidar site, and one was aboard the *Silver Prince.* Obviously data from this last station were available only when the vessel was on station, that is, for daylight hours on eight weekdays. On most days the wind direction data from the surface station aboard the *Silver Prince* were unreliable.

The *Silver Prince* was generally stationed between 10 and 15 km due west of the lidar site. In addition to providing surface observations, the ship was the site of the launching of 28 rawinsondes during the project. Temperature, humidity, and pressure were measured by the VIZ W-8000RP+ package at ~50-m height intervals, and the package also received Loran-C signals from which horizontal winds were determined. NPS personnel launched these sondes at 2-h intervals and terminated them at 50-kPa altitude. Participants from Louisiana State University launched a second set of radiosonde ascents from the primary sodar site. They produced 27 thermodynamic soundings during LASBEX on a schedule that coincided with interesting lidar observations. Upper-level winds were provided by lidar VAD scans, as described in section 2a.

In addition to observations by the instruments specifically deployed for LASBEX, surface observations are taken routinely at a number of sites in the Monterey Bay vicinity, as indicated on Fig. 1a. Yetter (1990) described these sites and the type of data available from each, and Shaw and Lind (1989) compiled data from these sources, as well as the radiosonde and surface mesonet data, for the LASBEX period.

Although we do not have seawater temperatures, the average ship-, buoy-, and satellite-derived temperature of the water surface in Monterey Bay during September 1987 was 14°–15°C (NESDIS 1987). The air temperature just above the surface of the water is also available from rawinsonde and surface mesonet stations aboard the *Silver Prince.* The temperature from the lowest observation of each of the 26 radiosonde profiles, taken on the 8 days when the ship was on station, averaged 13.9°C and ranged between 11° and 16°C. Surface mesonet station observations from the ship also fell between 11° and 16°C. Data from both the National Environmental Satellite Data and Information Service (NESDIS) and the *Silver Prince* are thus consistent with a surface temperature near 14°C.

b. Doppler sodars

The plans for LASBEX called for the deployment of three Doppler sodar systems in a triangle 1.5 km apart, referred to on Fig. 1 as the sodar triangle. Two of the sodars were at their planned positions for only part of the time, however. The sodar at the westernmost vertex of the triangle was near a noisy highway, which

interfered with the sodar signal. This sodar was moved to the lidar site on 25 September. The sodar at the easternmost vertex of the sodar triangle operated only from 25 to 29 September. At the northernmost vertex of the triangle, the "primary sodar site," participants from The Pennsylvania State University operated a sodar continuously for the entire project (except for a few short periods when power was lost at the site). Further details on the operation of the sodars were given by Intrieri et al. (1990), Fagan (1988), and Yetter (1990).

REFERENCES

Arritt, R. W., 1989: Numerical modeling of the offshore extent of sea breezes. *Quart. J. Roy. Meteor. Soc.*, **115**, 547–570.

——, 1991: A numerical study of sea breeze frontogenesis. Preprints, *Fifth Conf. on Meteorology and Oceanography of the Coastal Zone*, Miami, Florida, Amer. Meteor. Soc., 16–29.

Atkinson, B. W., 1981: *Mesoscale Atmospheric Circulations*. Academic Press, 125–214.

Atlas, D., 1960: Radar detection of the sea breeze. *J. Meteor.*, **17**, 244–258.

Banta, R. M., L. D. Olivier, E. T. Holloway, R. A. Kropfli, B. W. Bartram, R. E. Cupp, and M. J. Post, 1992: Smoke column observations from two forest fires using Doppler lidar and Doppler radar. *J. Appl. Meteor.*, **31**, 1328–1349.

Browning, K. A., and R. Wexler, 1968: The determination of kinematic properties of a wind field using a Doppler radar. *J. Appl. Meteor.*, **7**, 105–113.

Conrad, V., 1928: Beobachtungen über den Seewind an einem flachen Sandstrand. *Ann. Hydrogr., Berl.*, **56**, 1–3.

Dalu, G. A., and R. A. Pielke, 1989: An analytical study of the sea breeze. *J. Atmos. Sci.*, **46**, 1815–1825.

Defant, F., 1951: Local winds. *Compendium of Meteorology*, Amer. Meteor. Soc., 655–672.

Estoque, M. A., 1961: A theoretical investigation of the seabreeze. *Quart. J. Roy. Meteor Soc.*, **87**, 136–146.

——, 1962: The sea breeze as a function of the prevailing synoptic situation. *J. Atmos. Sci.*, **19**, 244–250.

Fagan, M., 1988: The sea breeze circulation during the Land Sea Breeze Experiment (LASBEX) in central California. M.S. thesis, Department of Meteorology, Naval Postgraduate School, Monterey, California 93943-5000, 127 pp.

Fett, R. W., and P. M. Tag, 1984: The sea-breeze-induced coastal calm zone as revealed by satellite data and simulated by a numerical model. *Mon. Wea. Rev.*, **112**, 1226–1233.

Fosberg, M. A., and M. J. Schroeder, 1966: Marine air penetration in central California. *J. Appl. Meteor.*, **5**, 573–589.

Frizzola, J. A., and E. L. Fisher, 1963: A series of sea breeze observations in the New York City area. *J. Appl. Meteor.*, **2**, 722–739.

Hall, F. F., Jr., R. M. Huffaker, R. M. Hardesty, M. E. Jackson, T. R. Lawrence, M. J. Post, R. A. Richter, and B. F. Weber, 1984: Wind measurement accuracy of the NOAA pulsed infrared Doppler lidar. *Appl. Opt.*, **23**, 2503–2506.

Hardesty, R. M., T. R. Lawrence, and R. E. Cupp, 1987: Performance of a 2-J/pulse injection-locked TEA laser for atmospheric wind measurements. *Conf. on Lasers and Electro-Optics Digest Series*, **14**, Baltimore, Optical Society of America, 128 pp.

——, R. E. Cupp, M. J. Post, and T. R. Lawrence, 1988: A ground-based, injection-locked, pulsed TEA laser for atmospheric wind measurements. *Proc. SPIE*, **889**, 23–28.

——, M. J. Post, and R. M. Banta, 1991: Observing atmospheric winds with a Doppler lidar. *Opt. Photonics News*, **2**, 12–15.

Intrieri, J. M., C. G. Little, W. J. Shaw, R. M. Banta, P. A. Durkee, and R. M. Hardesty, 1990: The Land/Sea Breeze Experiment (LASBEX). *Bull. Amer. Meteor. Soc.*, **71**, 656–664.

Johnson, A., Jr., and J. J. O'Brien, 1973: A study of an Oregon sea breeze event. *J. Appl. Meteor.*, **12**, 1267–1283.

Lyons, W. A., 1972: The climatology and prediction of the Chicago lake breeze. *J. Appl. Meteor.*, **11**, 1259–1270.

——, and L. E. Olsson, 1973: Detailed mesometeorological studies of air pollution dispersion in the Chicago lake breeze. *Mon. Wea. Rev.*, **101**, 387–403.

Menzies, R. T., and R. M. Hardesty, 1989: Coherent Doppler lidar for measurements of wind fields. *Proc. IEEE*, **77**, 449–462.

Meyer, J. H., 1971: Radar observations of land breeze fronts. *J. Appl. Meteor.*, **10**, 1224–1232.

Mohr, C. G., and L. J. Miller, 1983: CEDRIC—A software package for Cartesian space editing, synthesis, and display of radar fields under interactive control. Preprints, *21st Conf. on Radar Meteorology*, Edmonton, Alberta, Canada, Amer. Meteor. Soc., 569–574.

——, ——, R. L. Vaughn, and H. W. Frank, 1986: Merger of mesoscale data sets into a common Cartesian format for efficient and systematic analysis. *J. Atmos. Oceanic Technol.*, **3**, 143–161.

Nakane, H., and Y. Sasano, 1986: Structure of a sea-breeze front as revealed by a scanning lidar observation. *J. Meteor. Soc. Japan*, **64**, 787–792.

National Environmental Satellite Data and Information Service, 1987: *Oceanographic Monthly Summary*, **7**, 16 pp.

National Research Council, 1992: Coastal meteorology: A review of the state of the science. National Academy Press, 2101 Constitution Ave. NW, Washington, DC 20418, 99 pp.

Pielke, R. A., 1974: A three-dimensional numerical model of the sea breezes over South Florida. *Mon. Wea. Rev.*, **102**, 115–139.

——, 1984: *Mesoscale Meteorological Modeling*. Academic Press, 612 pp.

Post, M. J., 1978: Experimental measurements of atmospheric aerosol inhomogeneities. *Opt. Lett.*, **2**, 166–168.

——, and R. E. Cupp, 1990: Optimizing a pulsed Doppler lidar. *Appl. Opt.*, **29**, 4145–4158.

Rotunno, R., 1983: On the linear theory of land and sea breeze. *J. Atmos. Sci.*, **40**, 1999–2009.

Schroeder, M. J., M. A. Fosberg, O. P. Cramer, and C. A. O'Dell, 1967: Marine air invasion of the Pacific coast: A problem analysis. *Bull. Amer. Meteor. Soc.*, **48**, 802–808.

Shaw, W. J., and R. J. Lind, 1989: Sounding and surface meteorological data from the Land/Sea Breeze Experiment (LASBEX). NPS-63-90-001, 294 pp.

Stull, R. B., 1988: *An Introduction to Boundary Layer Meteorology*. Kluwer Academic, 666 pp.

Wakimoto, R. M., and J. C. McElroy, 1986: Lidar observations of elevated pollution layers over Los Angeles. *J. Climate Appl. Meteor.*, **25**, 1583–1599.

Wallington, C. E., 1960: Convection at the sea breeze front. *Cumulus Dynamics*, Pergamon Press, 119–125.

Yetter, J. A., 1990: The nature of the propagation of sea breeze fronts in central California. M.S. thesis, Department of Meteorology, Naval Postgraduate School, Monterey, California 93943-5000, 65 pp.